water MDPI

Article

Spatio-Temporal Variation in Suspended Sediment during Typhoon Ampil under Wave–Current Interactions in the Yangtze River Estuary

Jie Wang [1], Cuiping Kuang [1,*], Daidu Fan [2,*], Wei Xing [1], Rufu Qin [2] and Qingping Zou [3]

[1] College of Civil Engineering, Tongji University, Shanghai 200092, China; 2011141@tongji.edu.cn (J.W.); 2232336@tongji.edu.cn (W.X.)
[2] State Key Laboratory of Marine Geology, Tongji University, Shanghai 200092, China; qinrufu@tongji.edu.cn
[3] The Lyell Centre for Earth and Marine Science and Technology, Institute for Infrastructure and Environment, Heriot-Watt University, Edinburgh EH14 4AS, UK; q.zou@hw.ac.uk
* Correspondence: cpkuang@tongji.edu.cn (C.K.); ddfan@tongji.edu.cn (D.F.)

Abstract: Suspended sediment plays a major role in estuary morphological change and shoal erosion and deposition. The impact of storm waves on sediment transport and resuspension in the Yangtze River Estuary (YRE) was investigated using a 3D coupling hydrodynamic-wave model with a sediment transport model during Typhoon Ampil. This model has been validated in field observations of water level, current, wave, and sediment concentration. The model was run for tide only, tide + wind, tide + wind and wave forcing conditions. It was found that: (1) typhoons can increase the suspended sediment concentration (SSC) by enhancing bed shear stress (BSS), especially in the offshore area of the YRE, and there is hysteresis between SSC and BSS variation; (2) exponential and vertical-line types are the main vertical profile of the SSC in the YRE and typhoons can strengthen vertical mixing and reconstruct the vertical distribution; and (3) waves are the dominating forcing factor for the SSC in the majority of the YRE through wave-induced BSS which releases sediment from the seabed. This study comprehensively investigates the spatio-temporal variation in SSC induced by Typhoon Ampil in the main branch of the YRE, which provides insights into sediment transport and resuspension during severe storms for estuaries around the world.

Keywords: suspended sediment concentration; sediment transport model; Yangtze River Estuary; Typhoon Ampil

Citation: Wang, J.; Kuang, C.; Fan, D.; Xing, W.; Qin, R.; Zou, Q. Spatio-Temporal Variation in Suspended Sediment during Typhoon Ampil under Wave–Current Interactions in the Yangtze River Estuary. *Water* **2024**, *16*, 1783. https://doi.org/10.3390/w16131783

Academic Editor: Achim A. Beylich

Received: 3 June 2024
Revised: 16 June 2024
Accepted: 19 June 2024
Published: 24 June 2024

1. Introduction

Estuaries between land and sea are subject to complex interactions of runoff, tide, wave and wind, and spatio-temporal variations [1]. In recent years, climate change and global warming have increasingly been recognized as drivers of the rise in natural disasters. The frequency and intensity of coastal weather extremes such as heat waves, floods [2], and typhoons [3–5] have the potential to aggravate disaster risks in coastal cities. Furthermore, the impacts of climate change on ecosystem functions may exacerbate geological hazards, leading to changes in material distribution and estuarine geomorphology [4,6]. Currently, typhoons are one of the most damaging extreme events in coastal areas, characterized by powerful winds and waves. These events not only cause loss of life and direct economic losses but also cause the disruption of human activities [7–10]. The impacts of typhoons in estuarine regions primarily manifest in water environment change, sediment transport, erosion, dynamic responses, and the distribution of suspended material, all of which can have cascading effects on economic development. Overall, typhoons can trigger heavy precipitation, storm surges [11,12], and large waves [13] and impact wetland ecosystems [11,14]. Most estuaries are exposed to the open sea. The magnitude of storm damage in estuaries has significantly increased [15,16].

Suspended sediment concentration (SSC) plays a vital role in changing geometry and causing deposition/erosion, therefore jeopardizing the safety of ports, wharves, and dams and threatening lives near the estuary. Previous studies show that sediment erosion/deposition and transport in estuarine areas are controlled by many factors [1,17–22], i.e., tropical cyclones, strong currents, salinity variation, submarine topography, and river runoff [23–28]. The bottom shear stress induced by storm waves is one of the main driving forces for sediment suspension, and the wave period and water depth determine the intensity of bottom shear stress [29]. He et al. (2013) [30] found that typhoons can increase the SSC for a limited time interval. Xu et al. (2020) [31] proposed the four deposition mechanisms in the Yangtze River Estuary (YRE), i.e., the flow expansion, residual current, riverbed thalweg orientation, and local circulation act in different positions. Despite a significant number of studies dedicated to this problem, the dynamics of suspended sediment transport and the mechanism caused by deposition/erosion remain not fully understood.

Typhoons affect estuary morphology through sediment transport and the morphological evolution of shoals [32–34]. Time and space variations in hydrodynamics forcing during the typhoon period drive sediment transport and form erosion or deposition [35–37]. The large amount of sediment transport and suspension increases the shoal width and causes channel siltation [34,38,39]. Waves and tidal currents contribute jointly to bottom-deposited sediment resuspension [40], i.e., waves suspend the sediment and currents transport it. Schoellhamer (1996) [29] observed that wind and waves are the main forces in suspending sediment, and the frequency and extent of suspension were decided by the wind direction in a shallow microtidal estuary. The field observations by Bian et al. (2013) [36] indicate that during typhoons, a large amount of sediment was resuspended due to wave actions in the Yellow Sea and the East China Sea. Due to difficulties in collecting field observation data during severe storms, comprehensive studies on the influences of typhoons on SSC still remain to be explored.

The YRE is one of the most important estuaries in China and the world due to its massive water discharge and sediment concentration [41–43]. The construction of projects in the upstream area has resulted in a significant reduction of approximately 25–30% in the total sediment flux entering the sea [44], highlighting erosion as a global issue that attracts considerable attention. Given the challenges associated with expensive and constrained field observations and the intricate geomorphology of estuaries, numerical models have emerged as a prevalent method for studying the hydrodynamics, sediment transport, and morphodynamics of estuarine regions. After the first wave forecast model was implemented in the 1940s, the application of numerical methods gradually became widespread for coastal studies. Ma et al. (2009) [45] used the ECOMSED model to simulate the sediment transport of the macrotidal Mersey estuary in England and revealed the interplay between hydrodynamics, morphology, and the significant effects of both tidal level and river discharge on sediment transport. Zhu et al. (2016) [46] used a numerical model to study erosion in the Yangtze Delta and found that tides were the main driving force for erosion between 1997 and 2010. Li et al. (2016) [47] combined MODIS remote sensing and the Delft 3D model to investigate the effects of Super Typhoon Saomai on sediment erosion, re-suspension, transport, and deposition processes in the YRE.

In this study, a three-dimensional coupled hydrodynamic and sediment transport model was used to examine the hydrodynamics and suspended sediment transport in horizontal and vertical directions in real-world typhoon scenarios in the YRE. Typhoon Ampil is the third typhoon to land directly in Shanghai since 1949 and has the representative storm track and landing position. Originating as a severe tropical storm in the Pacific Ocean, Ampil traveled northwestward, ultimately hitting Chongming Island with a peak center wind speed of 28 m/s. The storm caused damage to 7200 homes, USD 246 million in economic losses, and the evacuation of 38,700 individuals (source: http://www.cjw.gov.cn/, accessed on 1 January 2022). Figure 1 shows the primary study area, study sites, and storm track of Ampil. The aims of this study are to investigate the characteristics of SSC during the typhoon period and assess the relative importance of the contribution of waves, wind, and currents to suspended sediment transport. The study of variation in SSC in the YRE during Typhoon Ampil not only provides a better understanding of the water–sediment transport mechanism but also an important basis for environmental protection, navigational channel management, and climate change adaptation.

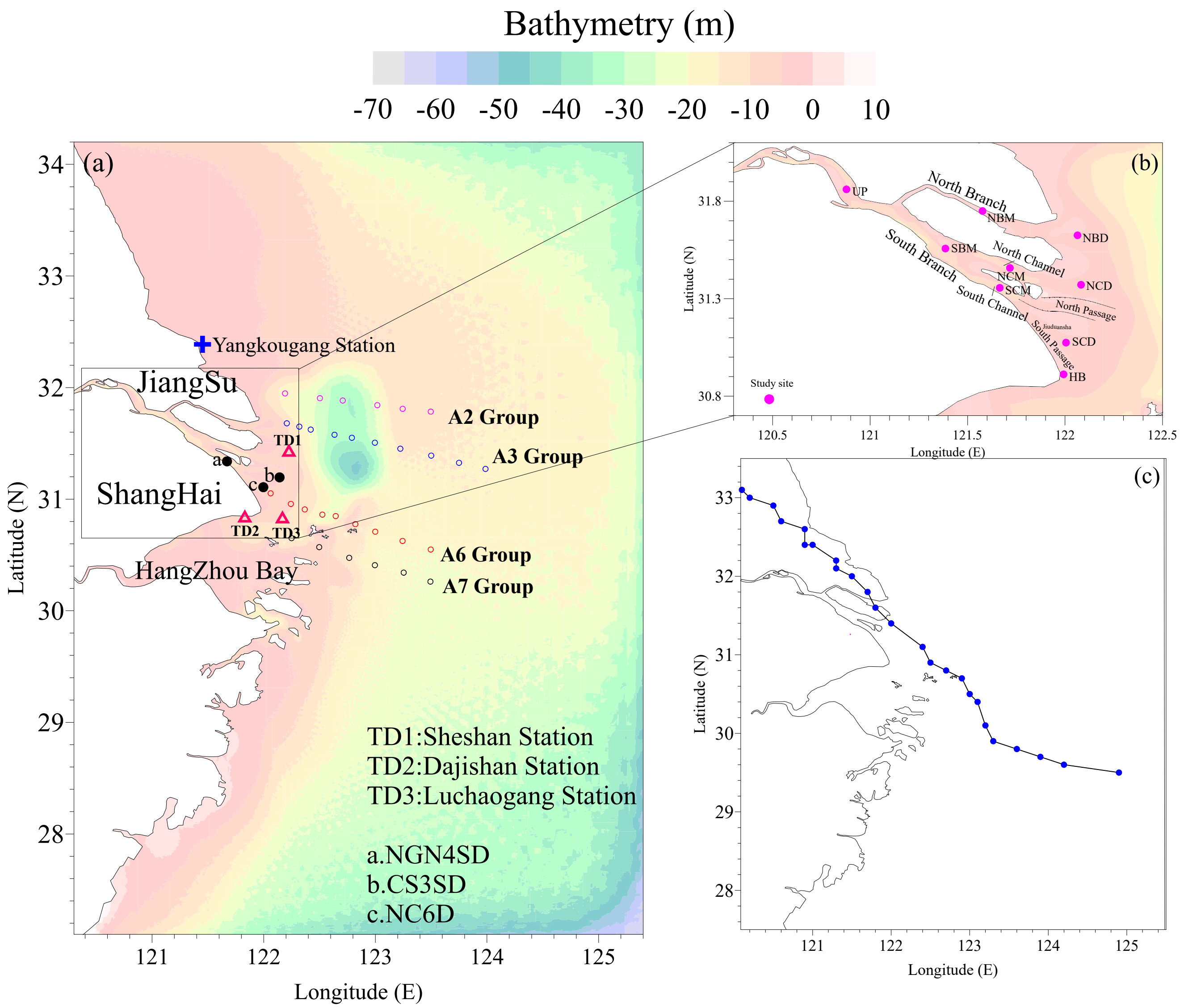

Figure 1. The study area and the storm track of Typhoon Ampil (2018). (**a**) Overview of the simulation area with the field stations of water level indicated by pink triangles, currents denoted by black solid circles, and the ship measurement point of sediment denoted by the four groups of hollow circles. (**b**) The focus study area with its main branches; the nine pink solid circles are the main study point in the following analysis and the typhoon path of Ampil. (**c**) The storm track of Typhoon Ampil moving from the East China Sea in the northwest direction.

2. Numerical Model

In this study, a 3D hydrodynamics model based on MIKE3 was developed by the DHI Group [48], which utilizes a flexible unstructured mesh to simulate the hydrodynamics and sediment transport affected by Typhoon Ampil. The hydrodynamics and sediment transport modules of the MIKE FLOW Model were coupled with the spectral wave module to investigate the time and spatial variations in water level, current, wave, and suspended sediment concentration during the occurrence of Typhoon Ampil.

2.1. Hydrodynamic Model

To improve modeling accuracy and mitigate sensitivity to boundary conditions, the model domain encompasses Hangzhou Bay (HB) and the YRE to capture the intricate connections effectively. Encompassing a region spanning 26.9° N to 34.4° N and 120.2° E to 125.6° E, the study area extends 810 km in the north–south direction and 500 km in the west–east direction, as depicted in Figure 1.

In the horizontal plane, an unstructured triangular mesh, comprising 18,887 nodes and 33,656 elements, is employed. The mesh resolution gradually decreases from 33,000 m at the eastern open boundary to 10 m at the YRE channel to strike a balance between computational accuracy and efficiency, as illustrated in Figure 2. Owing to the complex geometry of the primary study area, the water column was divided into 10 vertical layers within the Sigma coordinate system, each with a relative water depth of 0.1. This approach accommodates the complex coastal bathymetry and bottom roughness effectively.

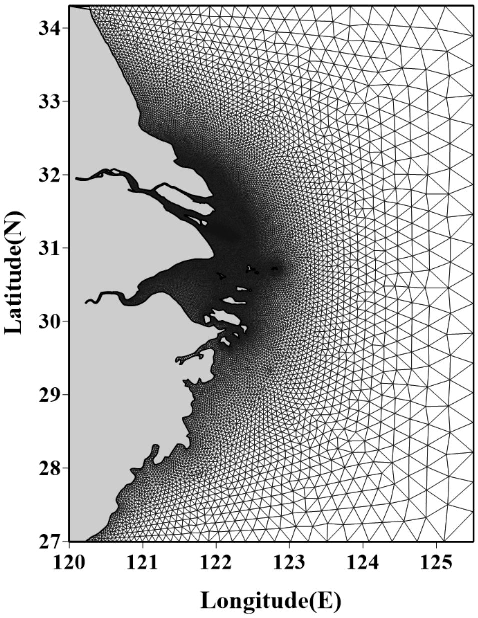

Figure 2. The unstructured grid system used in this study.

The bathymetry in the YRE and HB were sourced from the high-resolution charts of the People's Liberation Army Navy and remote sensing data provided by the National Oceanic and Atmospheric Administration (NOAA). Given the broad expanse of this geographical domain, the open boundaries (north, east, and south) were stimulated using time-varying tidal level data from the Global Tidal Model by MIKE3 [48]. Daily river discharge data from the Changjiang Sediment Bulletin (http://www.cjh.com.cn, accessed on 1 January 2022) were utilized for calculating the annual average discharge of the Jiangyin River as the river boundary condition and similarly for the average annual discharge of the Qiangtang River (1000 m^3/s) for Cangqian.

The hydrodynamic model was enforced by the ERA5 wind data from the European Centre for Medium-Range Weather Forecasts (ECMWF) at 6 h intervals with a spatial resolution of 0.25° × 0.25°. Depth thresholds were set at values of 0.005 m, 0.05 m, and 0.1 m. The bottom roughness height (k_s) was calculated using the Manning coefficient. The input file for the distribution of k_s values ranging from 0.00027 m to 0.0016 m within the domain was derived from successive calibrations conducted by Chen et al. (2016) [49].

2.2. Sediment Transport Module

The sediment transport module describes the process of the erosion, transport, and deposition of sand/mud mixtures under the interaction of currents and waves, and salt flocculation can also be included in this module. The three-dimensional sediment convection–diffusion equation is described by:

$$\begin{aligned}&\frac{\partial c}{\partial t}+\frac{1}{\sqrt{G_{xx}}}\frac{\partial uc}{\partial x}+\frac{1}{\sqrt{G_{yy}}}\frac{\partial vc}{\partial y}+\frac{\partial(\omega-\mathrm{w}_s)c}{\partial z}-\frac{1}{\sqrt{G_{xx}}}\frac{\partial}{\partial x}\left(\varepsilon_x\frac{\partial c}{\partial x}\right)\\&-\frac{1}{\sqrt{G_{yy}}}\frac{\partial}{\partial y}\left(\varepsilon_n\frac{\partial c}{\partial y}\right)-\frac{\partial}{\partial z}\left(\varepsilon_z\frac{\partial c}{\partial z}\right)=0\end{aligned} \tag{1}$$

where c is the suspended sediment concentration (kg/m^3), u and v are the flow velocity in the x and y directions, w_s is the settling velocity of suspended sediment (m/s), and ε_x, ε_y and ε_z are the dispersion coefficients of the x, y, and z directions (m/s^2).

In this model, the main sediment transport parameters for the sand module were selected following those of Ren (2020) [50], who conducted lots of experiments as summarized in Table 1.

Table 1. Summary of the main parameters in the sediment transport module.

Parameter	Value
Density of sediment (kg/m^3)	2650
Density of the bed layer (kg/m^3)	800
Settling velocity (m/s)	0.0003
Erosion coefficient (kg/m^2/s)	5×10^{-5}
Erosion critical shear stress (N/m^2)	0.2~0.6
Deposition critical shear stress (N/m^2)	0.1

2.3. Wave Module

The dynamics of waves are described by the transport equation of wave action density. Wave spectrum evolves in time and space and is a function of angular frequency and wave direction. The wave action is related to the energy density by the equation:

$$N(\sigma,\theta)=\frac{E(\sigma,\theta)}{\sigma} \tag{2}$$

In this model, the main parameters were chosen following those of Wang et al. (2022) [51]. It is worth noting that due to the deviation between the observed and ECWMF-ERA-Interim wind [52–54], the latter was multiplied by a correcting factor of 1.3 following the method of Fan (2019) [53]. Table 2 shows the vital parameters of the wave module.

Table 2. Summary of the main parameters in the wave module.

Parameter		Value
Wave breaking		0.8
Bottom friction		0.00025
White capping	C_{ds}	4.1
	δ	0.5
Initial condition		JONSWAP wave

2.4. Model Validation

Model performance assessment entails the utilization of root mean square error (RMSE) and skill [55]. RMSE is a commonly employed statistical measure, which serves to quantify the magnitude of discrepancies between model outputs and observed data. Skill serves as an indicator of the level of agreement between the model and data. These metrics are defined as follows.

$$RMSE=\sqrt{\frac{\sum_i^n\left(\eta^i_{measured}-\eta^i_{simulated}\right)^2}{n}} \tag{3}$$

where $\eta^i_{measured}$ is the ith measured variable; $\eta^i_{simulated}$ is the ith simulated variable; and n is the total number of data points. A low RMSE means better model agreement with the data. Of note, 0.5 is often taken as the critical value to evaluate the model's accuracy.

$$Skill = 1 - \frac{\sum_{i=1}^{N} |M_i - D_i|^2}{\sum_{i=1}^{N} \left(|M_i - \overline{D}| + |D_i - \overline{D}|\right)^2} \tag{4}$$

where M_i and D_i are the ith model prediction and measurement data; $\overline{D}$ is the mean value in situ measured data; and N is the number of observations. The simulation is more accurate when the value of *skill* approaches 1 within 0.65~1.

Validation of this model was carried out by Wang et al. (2024) [56], and the model parameters were adjusted during the typhoon period to agree with the observations better. The water level data were collected from the three oceanic stations (Sheshan, Luchaogang, and Dajishan) operated by the State Oceanic Administration. The historical wave data were acquired from the 3 m buoy located at Yangkougang Station, which is also operated by the State Oceanic Administration. The sediment transport module uses the voyage measurements in the YRE (NORC2014-07) in July 2014 at four series of cruise points.

Figure 3 illustrates the validation of the predicted water level with the measured data. To ensure model accuracy, the validation period spans the duration of a typhoon passing through from 17 to 25 July 2018. Comparing the model predictions with the actual measurements, a slight deviation was observed at the three stations on 22 July. Upon integrating the assessment metrics with the temporal variations in the time series data, the RMSE indicates a marginal deviation of 0.3 m, which was in the measurement allowance of hydrology specification (within ±0.30 m), indicating that the model demonstrates the ability to accurately predict the real water levels.

(a) Sheshan Station

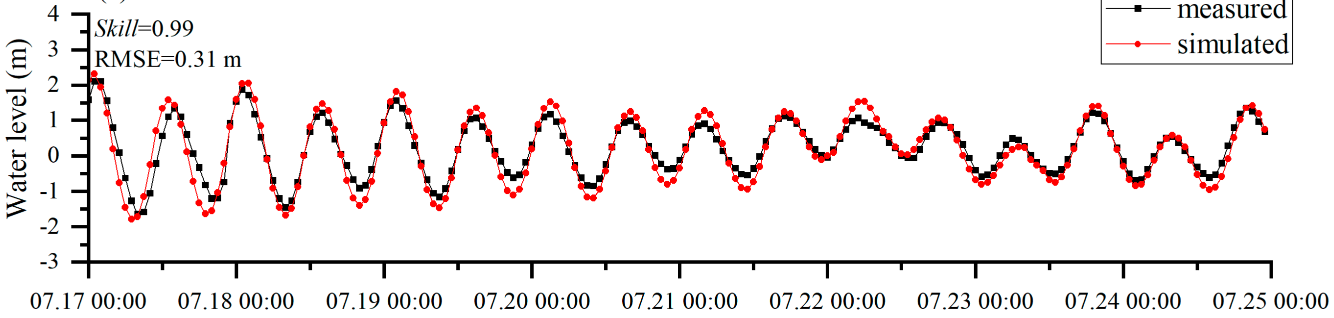

(b) Luchaogang Station

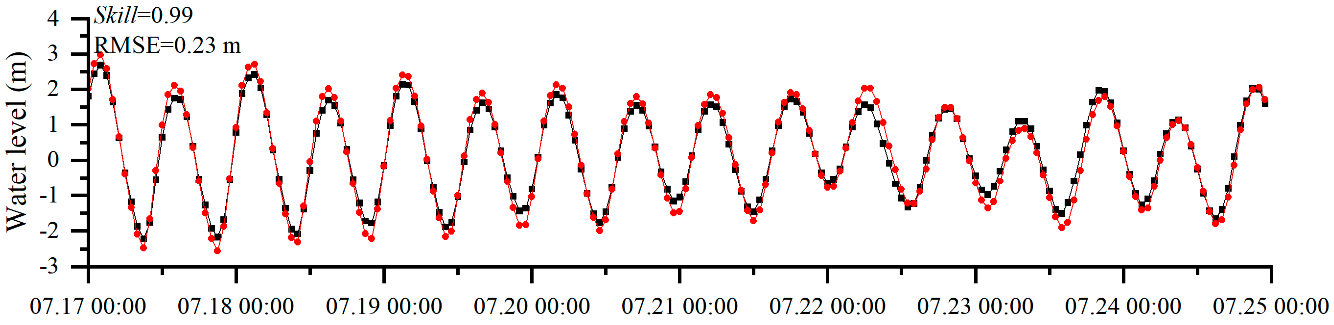

Figure 3. *Cont.*

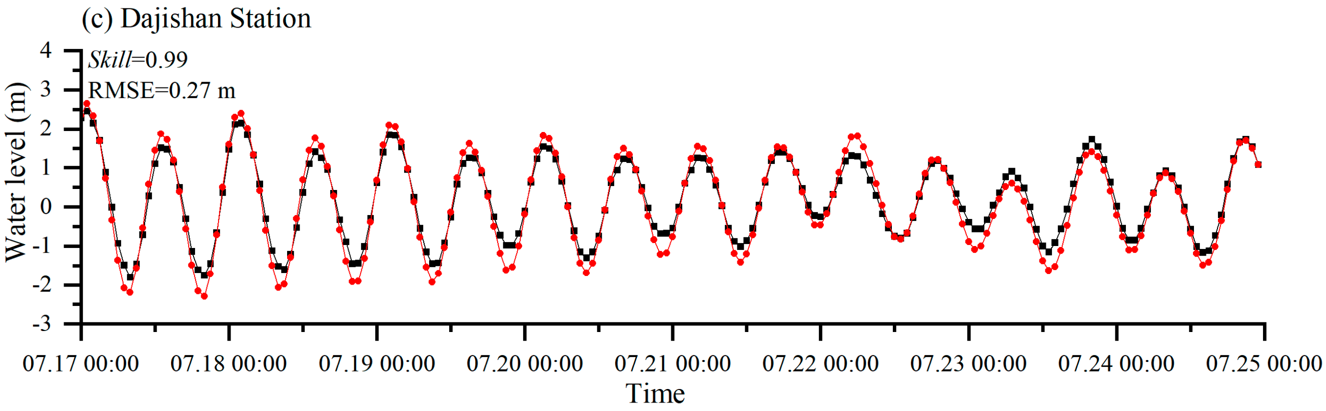

Figure 3. Comparison of simulated and measured water levels during Typhoon Ampil at the Luchaogang, Sheshan, and Dajishan field stations; the *skill* number and RMSE are shown in the figure.

The wave module uses the time series data from Yangkougang Station. The validated wave model was executed for the timeframe spanning 15 August to 1 October 2014, with the outcomes depicted in Figure 4. Analysis of the results revealed that discrepancies primarily manifest post typhoon landfall, indicating a reduction in wave height that agrees well with the measured data during the typhoon period. Although the significant wave height fails to reach the peak values observed in the measurements, the period exhibits concordant values following typhoon passage. It is acknowledged that acquiring measurements during a typhoon event faces challenges due to the intense winds and waves; thus, the deviations are deemed reasonable. The *skill* and RMSE values of wave height are 0.82 m and 0.43 m, and the wave periods are 0.92 s and 0.33 s, respectively, indicating the comprehensive accuracy of wave module performance.

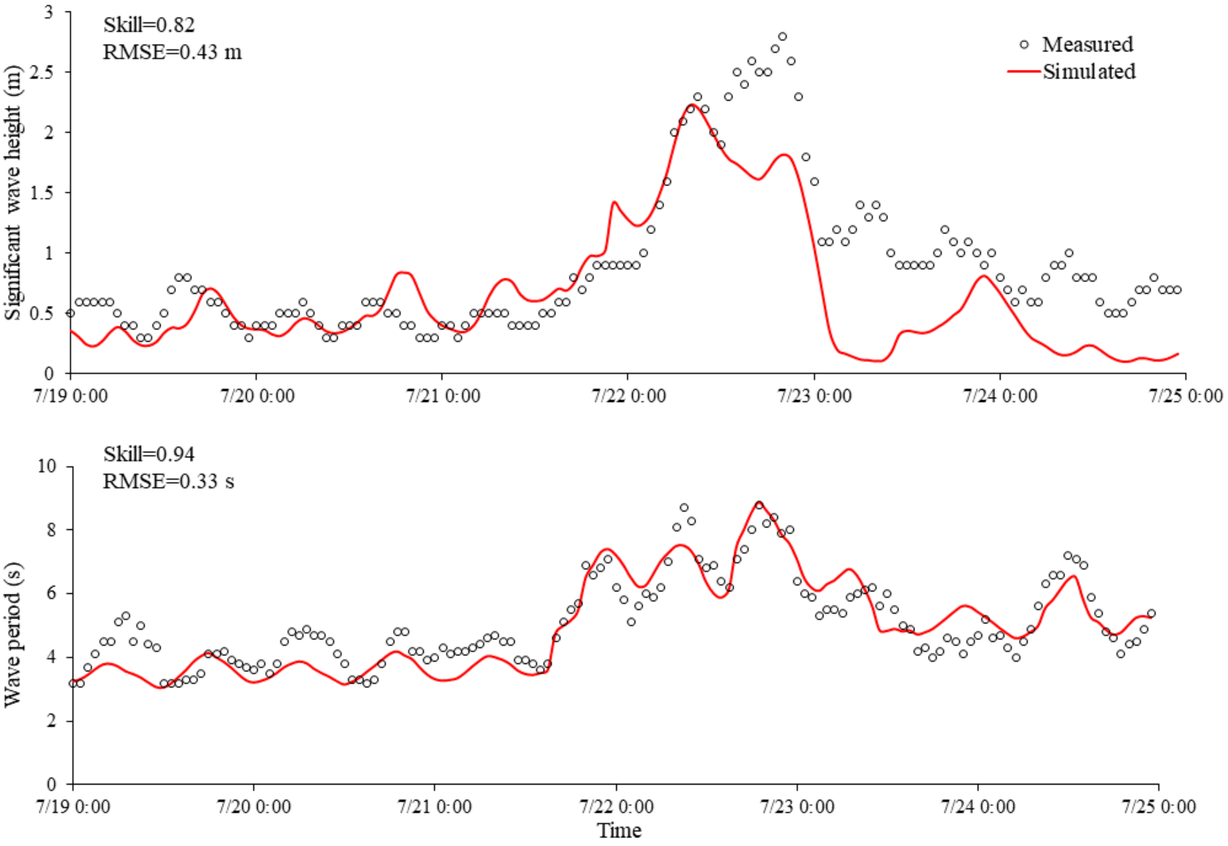

Figure 4. Validation of wave predictions during Typhoon Ampil at Yangkougang Station.

Given the sporadic characteristics of the collected measurements at various time points and locations, RMSE was employed as the primary performance metric for this module. Figure 5 presents the comparison between the model's results and measured data for surface and bottom SSC. While the model demonstrates a slight tendency to overpredict the measured values, the RMSE remains well within an acceptable range, indicating a satisfactory level of simulated performance.

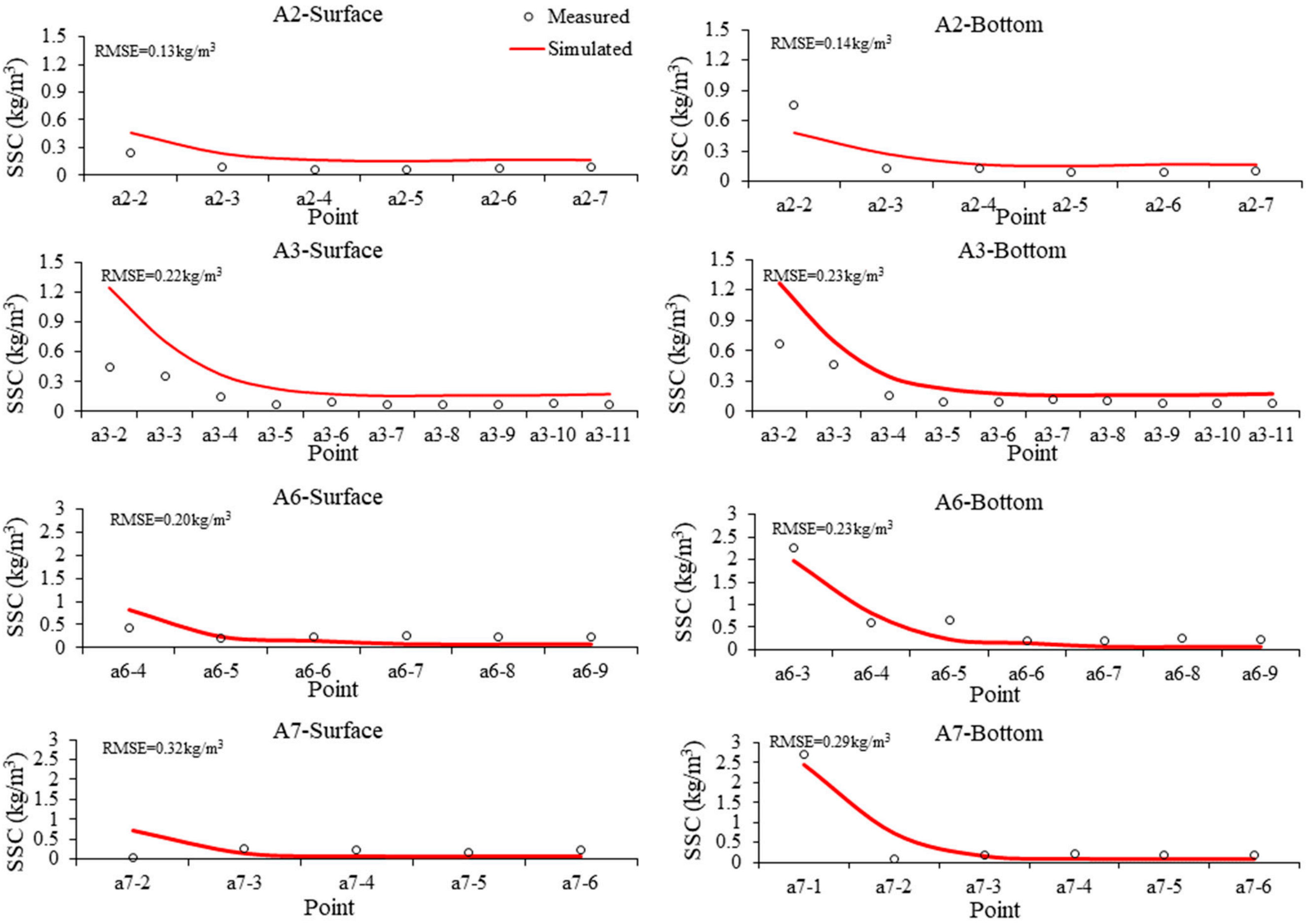

Figure 5. Validation of predicted suspended sediment concentration (SSC) using field observations collected by ships at the four groups of measured points indicated in Figure 1.

The wave and sediment transport module deviated from the observation during the typhoon period. Specifically, the model exhibited an overestimation of the observed SSC near the estuarine mouth. This discrepancy may be induced by the inaccuracies in the conversion equation utilized for turbidity (NTU) to concentration (kg/m^3) and the constant value of critical shear stress (CSS) used in model initialization. Additionally, the model's predictions indicated higher wave height and shorter periods compared to the observations following typhoon landfall, potentially attributed to the intricate and dynamic nature of typhoon wind fields not adequately captured by the ECMWF-ERA5 wind data. Considering that real situations entail more involute dynamics that can significantly affect these factors, the simulated results of the hydrodynamic and sediment transport model are concordant with the measured data, basically indicating that this 3D model effectively replicates real conditions.

3. Results

The model simulations were conducted over the period of 1 to 31 July 2018, following equilibrium by the coupled wave–current model before Typhoon Ampil landed. In this section, an analysis of the horizontal distribution and vertical mixing of SSC is performed to elucidate the common mechanism during typhoon passage. Figure 6 illustrates the wind velocity, water level, significant wave height, and period data obtained from Yangkougang Station during Typhoon Ampil. As Typhoon Ampil approached the YRE, a noticeable increase in wind speed, wave height, and period was observed, accompanied by heightened complexity in the wind field. The maximum wind speed at Yangkougang Station peaked at approximately 25 m/s, while the typhoon intensity was officially identified as grade 10 with a central speed of 28 m/s.

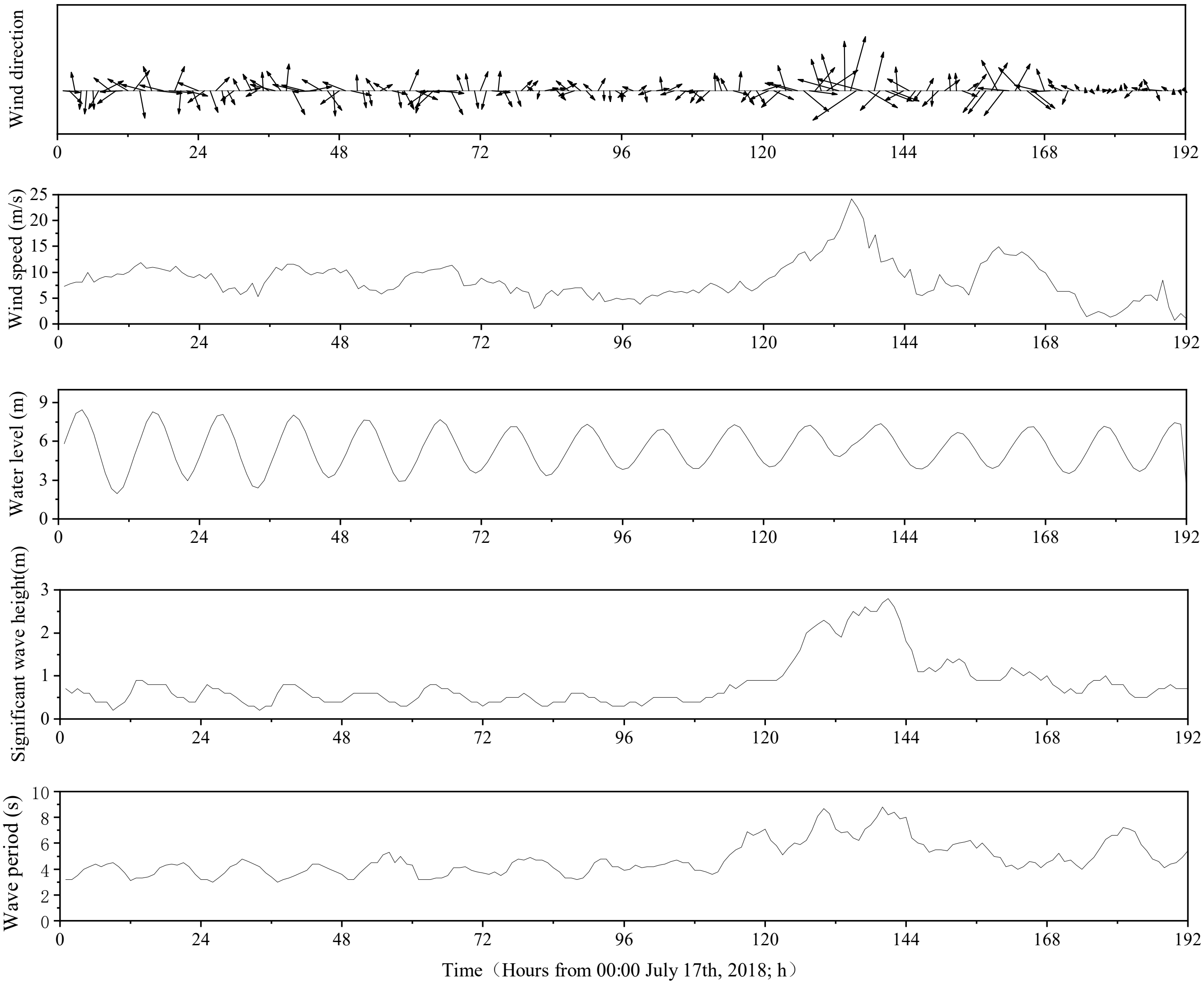

Figure 6. The measured wind velocity, water level, significant wave height, and period collected at Yangkougang Station as marked in Figure 1 during Typhoon Ampil (the time begins at 00:00, 17 July 2018).

3.1. Changes in SSC in the Main Study Area

In order to investigate the spatial variability of SSC in the primary branches of the YRE, nine specific study sites in the inner channel and offshore regions (as depicted in Figure 1) were selected during the typhoon event. In addition to the points representing the upstream area, the North Branch, North Channel, and South Channel, a point positioned between the YRE and HB along the coastline was also included to better capture the water exchange between the two estuaries. Among these points, UP represents the upstream position, NBM, SBM, NCM, and SCM represent mid-stream points in the North Branch, South Branch, North Channel, and South Channel, respectively, and NBD, NCD, and SCD correspond to points situated beyond the estuary mouth.

Figure 7 presents the temporal evolution of SSC at all selected study sites, with a blue arrow marking the approximate time of typhoon landfall (around 12:00, 22 July 2018). Analysis of the results shown in Figure 7 indicates minimal changes in SSC at UP, SBM, and SCM during the typhoon event, attributed to the relative insensitivity of these points to wind and wave influences. However, significant variations in SSC were observed at other study sites, deviating from the conventional expectation of a uniform increase. It is worth noting the substantial decrease in SSC at SCD following the arrival of Typhoon Ampil, a pattern similar to observations in the Modaomen estuary during typhoon Higos as documented by Liang et al. (2023) [57]. This decline can be explained by the interaction between flow patterns and wind forces. Highly concentrated sediment migrated over considerable distances in the predominant direction, leading to a rapid decrease at this site.

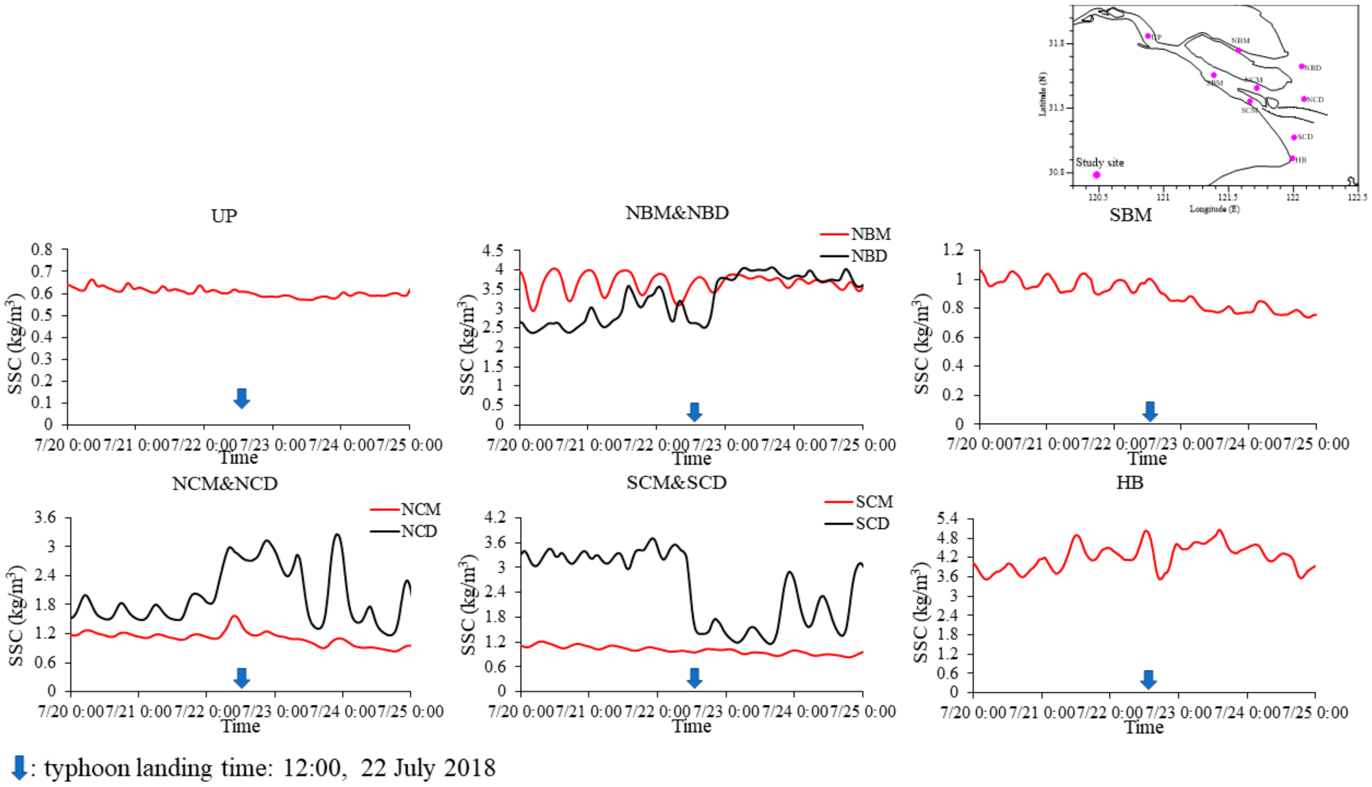

Figure 7. The time series from 20 to 25 July of surface suspended sediment concentration (SSC) at the nine selected study sites (as indicated in the top right corner).

SSC at the NBD initially decreased before rising to a peak value of 3 3.8 kg/m^3, representing a 52% increase from the normal value. In contrast, SSC at the HB experienced an initial increase followed by a 20% reduction. NCD exhibited a pronounced 90% rise in SSC relative to normal values, peaking at 3.3 kg/m^3. The SSC at the inner channel points, NBM and NCM, also experienced the impact of the typhoon event, with SSC escalating by 33.3% to reach a maximum value of 1.6 kg/m^3 at NCM upon typhoon landfall. The SSC at the NBM fluctuated slightly at a relatively high value, suggesting that the typhoon inhibited the tidal stress of the narrow channel.

To further assess what caused different SSC variations across the six points (NBM, NBD, NCM, NCD, SCD, and HB), we calculated four days of 24 h time-averaged SSC and constructed histograms illustrating the SSC trends alongside time-series data for bed shear stress (BSS) (refer to Figure 8). The BSS peaked concurrently with the typhoon peak intensity, with the rapid response to the strong winds and large waves. At NBD, NCD, and SCD, there was a discernible time lag of 6 to 24 h between the peaks of SSC and BSS, attributed to the time required for sediment to be resuspended from the seabed into the upper water columns. High SSC at SCD occurred earlier than at other points, implying that the typhoon path affects the SSC variation both temporally and spatially. Conversely, at the inner locations (NBM and NCM), the impact of the typhoon on BSS was minimal, exhibiting values lower than the CSS as depicted in Figure 7. This observation aligns with the shallowness and narrowness of the midstream area in the NB, resulting in weaker wind and wave actions, thus maintaining a BSS lower than the CSS required for sediment suspension. Consequently, SSC variations at these locations primarily correlate with tidal movements.

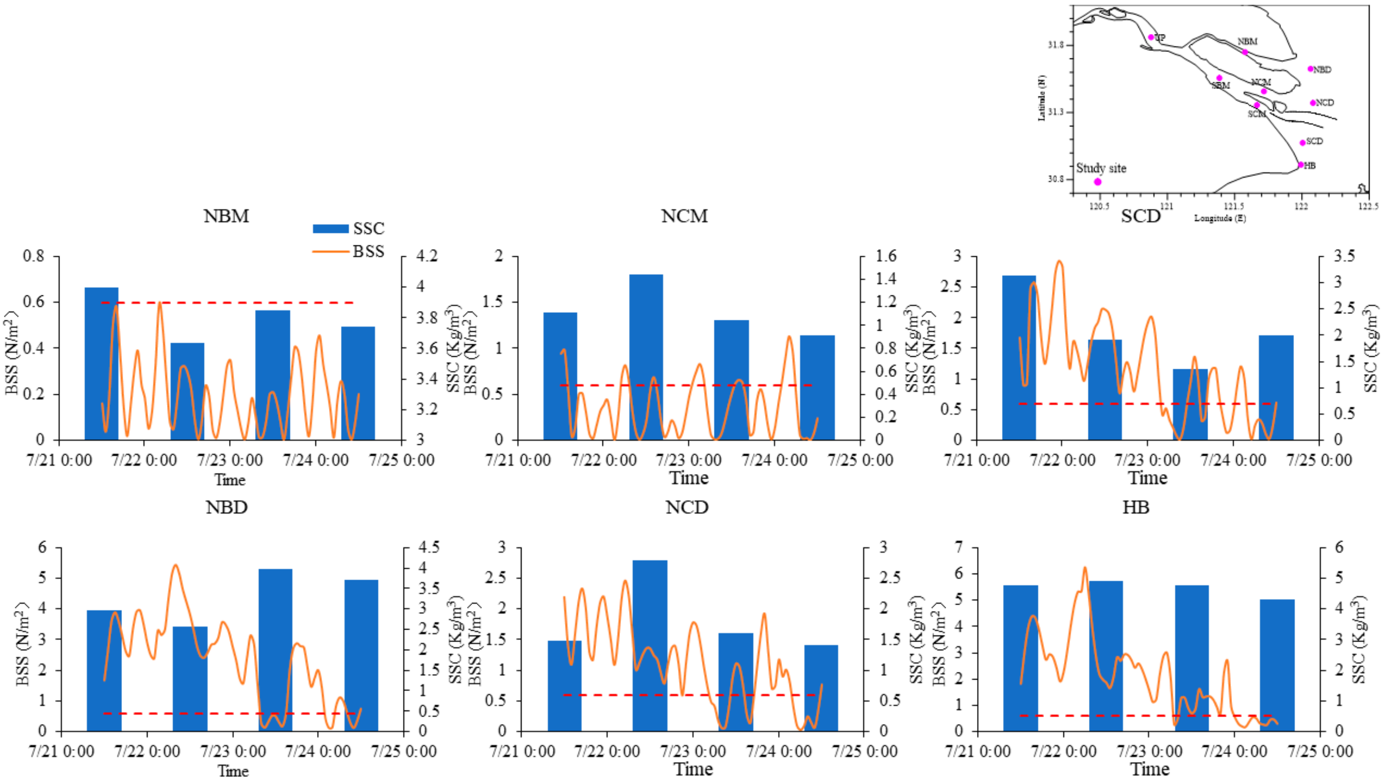

Figure 8. Bottom shear stress (BSS) variation and four 24 h time-averaged suspended sediment concentration (SSC) histograms before and after typhoon landing at the six selected study sites (the red dotted line represents the maximum critical shear stress).

3.2. The Characteristics of SSC Horizontal Distribution

As previously mentioned, the variation in SSC is different among the study sites during Typhoon Ampil. The distribution of surface SSC along with the current vector field is depicted in Figure 9. When comparing the four branches and the main stream, as shown in Figure 9, minimal changes in surface SSC are observed in the inner channel. This phenomenon can be attributed to two primary factors. Firstly, SSC in the channels is predominantly influenced by sediment inflow from the upstream region, which has decreased following the construction of the Three Gorges Reservoir, leading to reduced SSC variability. Secondly, runoff serves as the primary driver of SSC in the inner channel, while the impact of winds and waves is negligible in this particular area of the YRE.

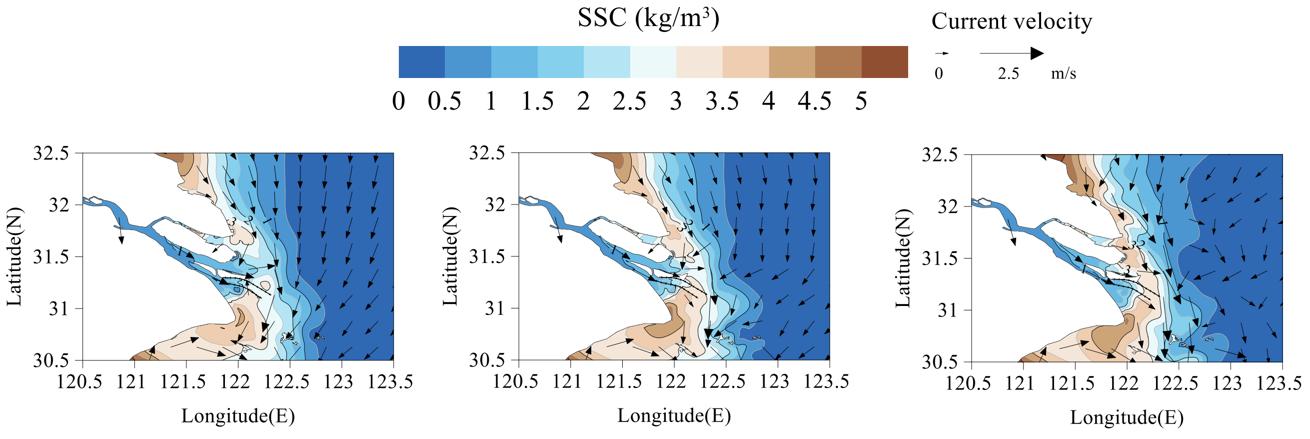

(a)July 21, 12 : 00 (b) July 22.00:00 (c) July 22, 12 : 00

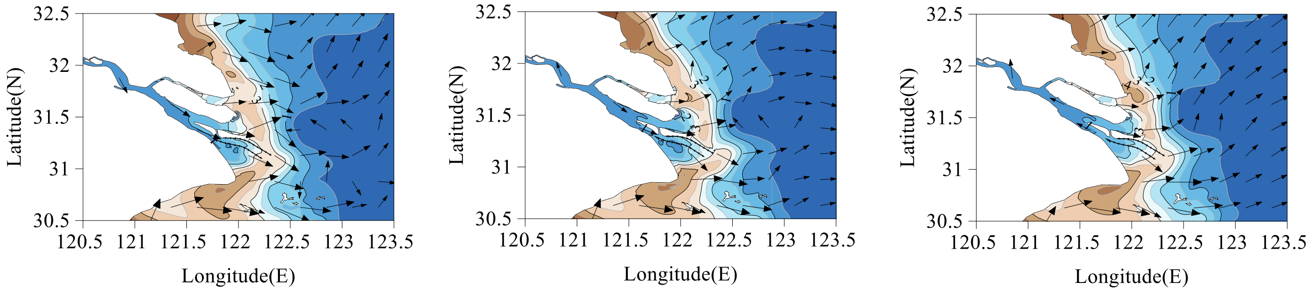

(d) July 23, 00 : 00 (e) July23, 12:00 (f) July 24, 00:00

Figure 9. Time evolution of horizontal variation in suspended sediment concentration (SSC) during the typhoon with the current vectors indicated by the arrows.

At the outer estuarine mouth, a high SSC zone, known as the turbidity maximum zone, is present due to the vertical mixing of salt and fresh water, resulting in elevated SSC values. When the typhoon approached the YRE, the SSC increased along the typhoon path, leading to significantly higher concentrations than those observed in the inner channels. Areas exposed to the open sea were more susceptible to the influence of strong winds and large waves compared to sheltered regions. Additionally, at the HB site, the high surface SSC was transported by strong currents toward the mouth of the South Passage (SP), subsequently reaching the North Channel (NC) along the typhoon path. The high surface SSC was a result of the interactions among wind, waves, and tides, involving various dynamic processes, notably the tidal currents (critical for sediment transport) and waves (the primary driver of sediment resuspension). This occurrence highlights how massive typhoon-induced waves disturb the water column, causing bottom sediment to resuspend into the sea surface. Furthermore, the complex movement of sediment during typhoon passage, combined with the influence of currents, can lead to sediment from shoals being dispersed into the surrounding waters, thereby enhancing the SSC values [58].

To be in agreement with the information mentioned in Section 3.1 about BSS, the corresponding horizontal variation in BSS is shown in Figure 10. The highest BSS levels were observed at the outer mouth of the estuary, coinciding with the turbidity maximum zone during the time of typhoon landfall. The findings suggest that the elevated SSC primarily originated from sediment resuspension from the seabed. Furthermore, they also indicate that the typhoon accelerates the exchange rate between deposition and suspended sediment, facilitating the uplift of the bottom sediment to the surface. The BSS at the inner channel varied only slightly and recovered to the normal value earlier than that further offshore, suggesting that SSC changes are dominated by current action.

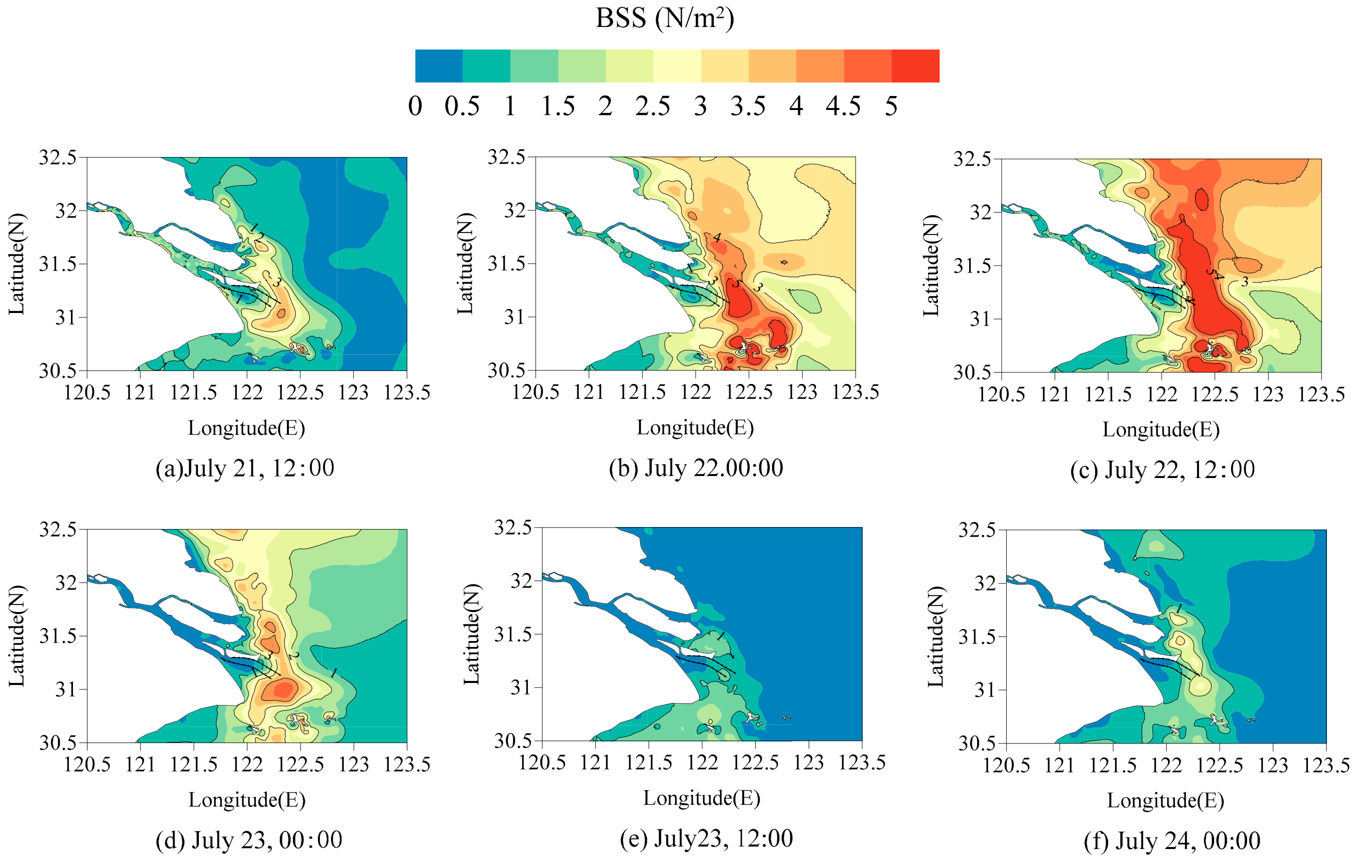

Figure 10. Time evolution of horizontal variation in bed shear stress (BSS) during Typhoon Ampil.

A comparison between the distribution of BSS and SSC in Figures 9 and 10 reveals that the time series (Figures 9d–f and 10d–f) corresponds to the period during which the typhoon passed and gradually moved away from the YRE with decreasing intensity. Despite this, SSC remained elevated compared to normal, whereas BSS began a rapid recovery toward normal values. It is widely accepted that winds and waves contribute to enhancing BSS. Consequently, the time lag between BSS and SSC is associated with hysteresis in the exchange of surface and bottom sediment. Due to weakened hydrodynamics after typhoons, the deposition of suspended sediment requires more time to settle back to the seabed before being resuspended. This phenomenon was also observed and called sedimentation hysteresis by Fan (2019) [59].

3.3. Vertical Distribution of SSC

Five types of vertical SSC profiles were summarized by Van Rijn (1993) [60], including exponential, oblique, vertical-line type, stepped, and two-layer structures. To further examine the mechanisms of suspended sediment transport, four sections indicated in Figure 11 along the main branches were selected to analyze the vertical distribution of suspended sediment during Typhoon Ampil and are depicted in Figures 12–15.

Figure 12 shows the spatial variation in SSC across NBL from 21 to 24 July with a time interval of 12 h. In most instances, the profile in this branch appeared as a vertical line, suggesting minimal concentration variations from the bottom to the surface. However, before the typhoon landed, the mouth area exhibited a slight exponential shape, with the bottom concentration slightly higher than that at the surface. During typhoon passage, sediment resuspension in the water column increased the exchange between surface and bottom components, leading to a gradual shift toward a vertical-line pattern. An additional phenomenon existing at the mouth area was the decrease in SSC by 1 to 1.5 kg/m^3 upon typhoon landfall at 12:00 on 22 July. This decrease was primarily attributed to the intense currents generated by the typhoon, which caused lower SSC water to flow into the channel along the typhoon's path. As the typhoon moved further away from the YRE, the SSC rapidly recovered to normal, with high SSC concentrations being carried out of the mouth by the ebb tide current, proving the transport function of the current. An obvious increase occurs at the range from 35,000 to 50,000 m of the relative distance, which was mainly caused by the increase in BSS that corresponded with the high SSC zone.

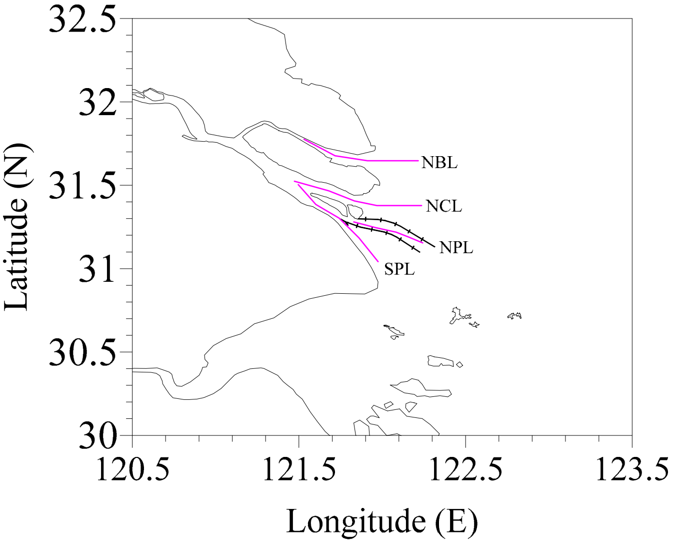

Figure 11. Four sections of NBL, NCL, CPL, and SPL along the main branches of the YRE for the analysis of the vertical distribution of suspended sediment during Typhoon Ampil.

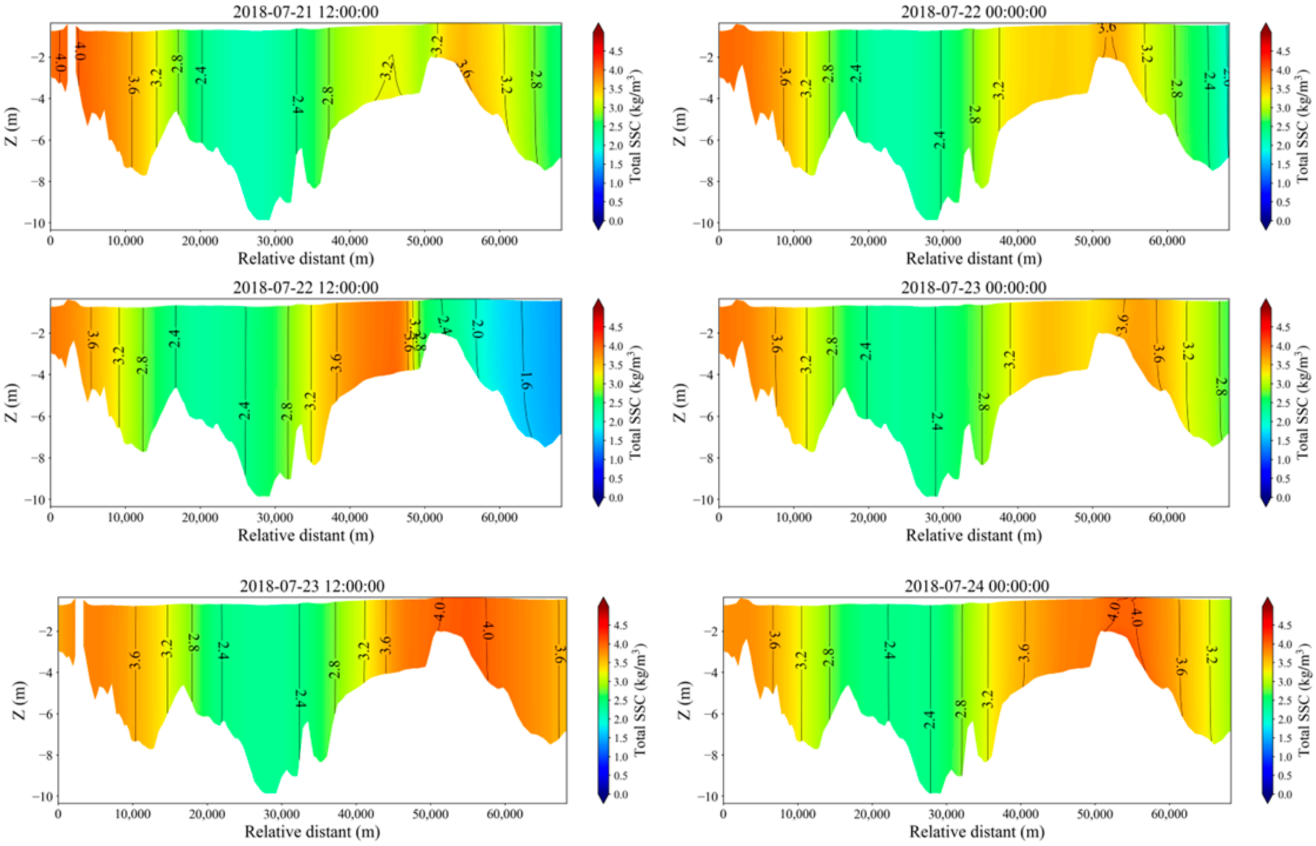

Figure 12. The spatial variation in suspended sediment concentration (SSC) across the section NBL indicated in Figure 12 from 21 to 24 July during Typhoon Ampil with a time interval of 12 h.

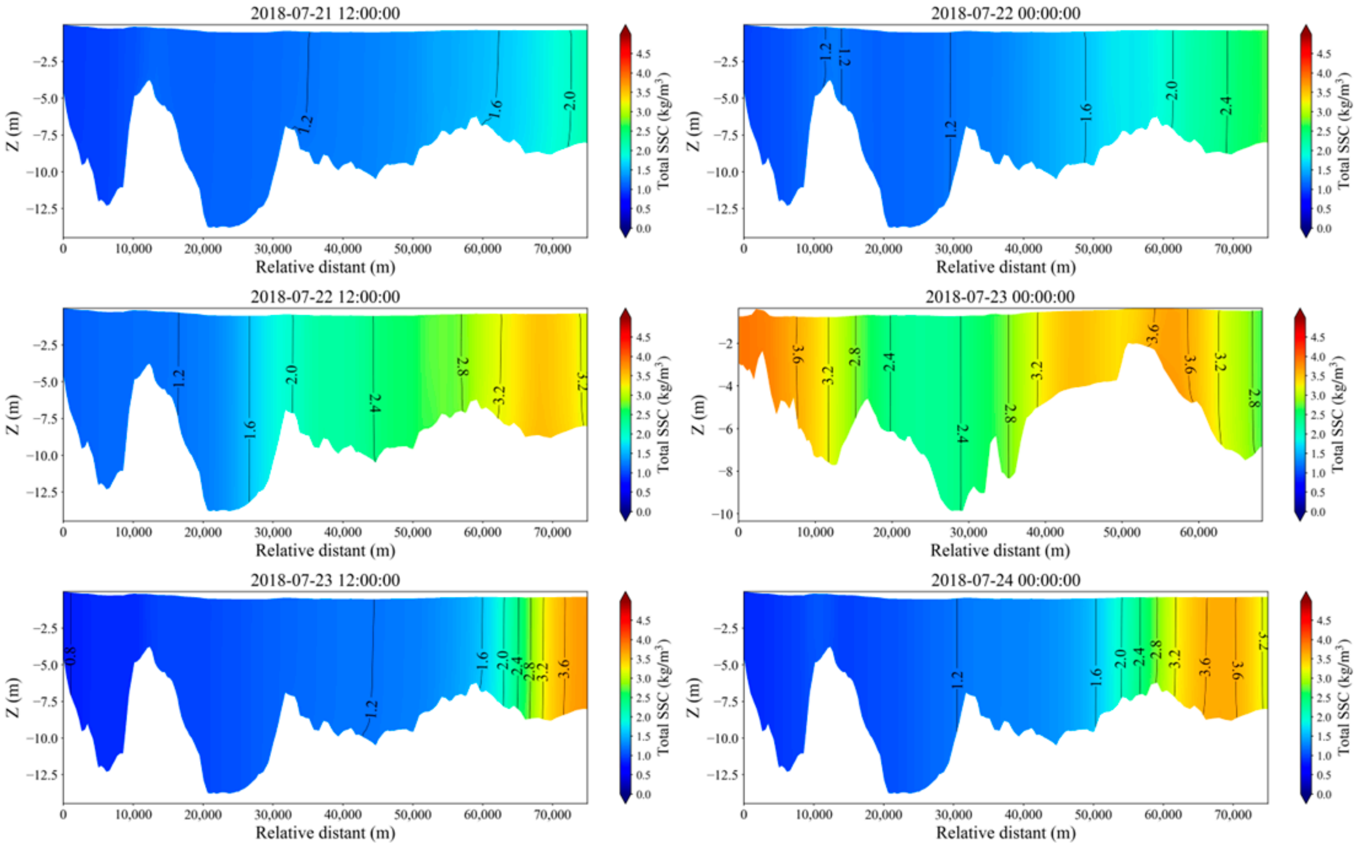

Figure 13. The spatial variation in suspended sediment concentration (SSC) across the section NCL indicated in Figure 12 from 21 to 24 July during Typhoon Ampil with a time interval of 612 h.

Figure 13 shows the spatial distribution of SSC across NCL at the same time as NBL. The SSC at NCL was lower overall than that at NBL. The SSC at NCL was generally lower compared to that at NBL. The vertical profile at NCL exhibited a transition from an exponential pattern to a more pronounced vertical-line pattern over a broader range, particularly in the relative distance of 10,000 to 60,000 m, indicating that the typhoon had the potential to enhance the vertical mixing process. Similarly, there was a notable rapid increase in SSC in the vertical direction at the mouth area. Within the distance range of 0 to 60,000 m, the primary influence came from tidal currents originating upstream, evident through the prompt recovery of SSC when the tide changed direction. However, the remaining driving force came from the interaction between current and storm waves that promoted seabed deposition resuspension, as indicated by the high SSC being slowly moved seaward, causing the fine isoline in the distance over 60,000 m.

Figure 14 exhibits the spatial variation in SSC across NPL, within the Deep-Water Channel project, an area influenced by intricate topography and complex current conditions. The vertical profiles between distances of 12,000 to 32,000 m appeared irregular, resembling the two-layer concept proposed by Van Rijn (1993) [60], characterized by distinct vertical current velocities. Furthermore, at the time of the typhoon making landfall (12:00 on 22 July 2018), the SSC remained nearly constant in the vertical direction, suggesting that strong winds and waves can reshape the vertical SSC structure through intense mixing and exchange between surface and bottom sediments.

The results in Figure 15 are the spatial variation in SSC across SPL. The vertical profile of SSC followed an exponential pattern with slight irregularities. The impact of the typhoon on SSC is less pronounced due to the typhoon's path passing through SP first. This observation highlights the significance of the typhoon's path relative to the study sites as a crucial factor influencing the storm's impact on suspended sediments. A similar trend was observed in NPL, where the typhoon track intersected later than in SPL. The lower SSC in NPL mitigates the typhoon's impact on vertical mixing compared to the other sections.

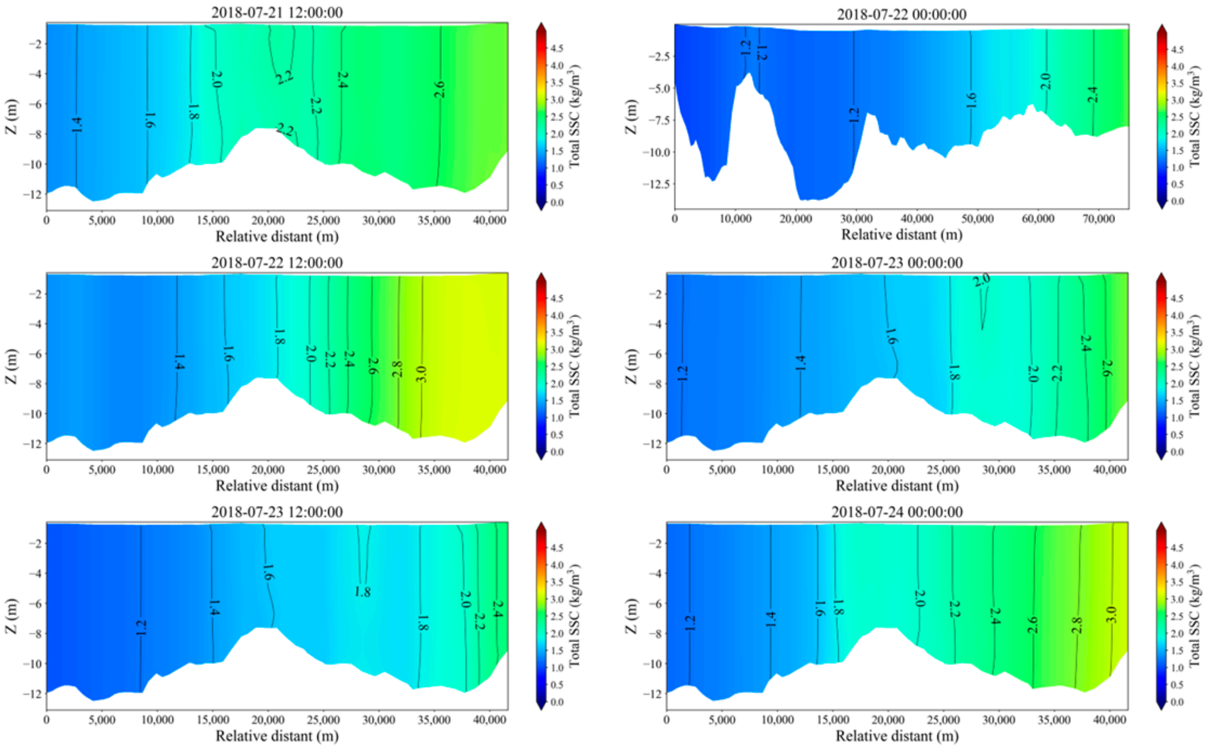

Figure 14. The spatial variation in suspended sediment concentration (SSC) across the section NPL indicated in Figure 12 from 21 to 24 July during Typhoon Ampil with a time interval of 12 h.

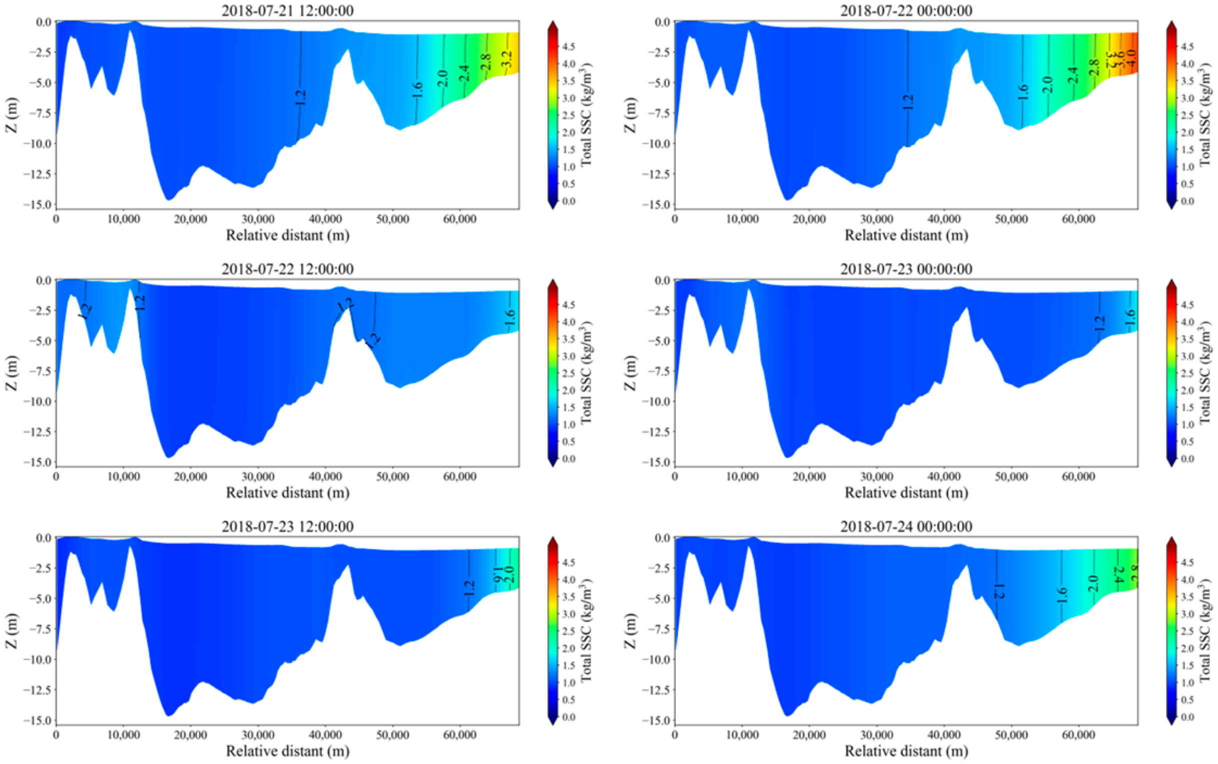

Figure 15. The spatial variation in suspended sediment concentration (SSC) across the section SPL indicated in Figure 12 from 21 to 24 July during Typhoon Ampil with a time interval of 12 h.

By comparing the four lines selected in the main branches, the vertical distribution of SSC can be succinctly summarized. The typical vertical profiles of SSC in the YRE are exponential type and vertical-line type, which are subject to modification by the influence of typhoons. Within the inner channels, SSC levels are primarily influenced by runoff and tidal currents, leading to SSC movement driven by these dynamics. The end of the section is within the high SSC zone, where the typhoon-enhanced BSS becomes the primary factor. The areas close to the estuarine mouth show complex vertical variation, due to the strong mass exchange and multiple dynamics. This result is consistent with the findings of Liu et al. (2010) [61], who studied the exchange rate between near-bottom and sea-bottom sediments.

4. Discussion

As we all know, wind plays a vital role in generating waves and strengthening ocean circulation. Therefore, wave impacts can also be attributed to wind function action. In a study by Li et al. (2019) [62], the researchers examined the effects of wave action on sediment resuspension both landward and seaward of the estuary. Accordingly, the model was set up for another two scenarios of the typhoon process with hydrodynamics forcing summarized in Table 3.

Table 3. Three scenarios of hydrodynamic forcing conditions.

Condition	Module	Dynamics	Scenario Name
1	Hydrodynamic	Tide only	Astronomic tide (AT)
2	Hydrodynamic	Tide + wind	Non-wave (NW)
3	Hydrodynamic + wave	Tide + wind + wave	Wave–current interaction (WCI)

4.1. Wave Impacts on SSC Distribution

Waves can increase the SSC in the short term by entraining sediments from the seabed, causing them to be suspended in the water, temporarily increasing the concentration of suspended sediments. During typhoon periods, large waves can drive intensive sediment transport and erosion, leading to a significantly high and temporally variable SSC in the water body [63], promoting accumulation and increasing SSC [64]. The influence of waves on the near-bottom suspended sediment concentration is most significant, with wave height or period determining the magnitude of suspended sediment concentration. Strong waves have a pronounced impact on the BSS on the seabed and, therefore, near-bed turbulence energy [65]. The WCI function is recognized for its potential contribution to sediment transport. Hence, this section explores the impact of waves on horizontal transport and the vertical exchange of sediment through different simulated scenarios of NW and WCI.

Figure 16 shows the horizontal SSC isolines changing with the typhoon path by comparing these two forcing conditions. For the NW condition, in general, the SSC is higher in the shoal areas than in the inner channels, with values close to 1.0 kg/m^3 in the eastern shoals of Chongming and 0.5 kg/m^3 in the SC and NC channels. When the wave force was added to the simulation, the concentration increased significantly with the isoline changing by 2.0 kg/m^3. The inner region has a lower SSC value of about 1.0 kg/m^3, which is twice as much as the NW condition, while SSC is increased by almost 20 times to almost 4.0 kg/m^3 in the shoal region. This phenomenon was the same as that observed by Lu et al. (2018) [66], who investigated the SSC variation in the East China Sea during Typhoon Chan-hom.

In addition to the concentration variation mentioned above, the duration required for the values to return to normal also showed variability based on the prevailing forcing conditions. Under the NW conditions, the recovery time was close to the typhoon path, indicating a prevalence of current-driven sediment transport. Incorporating wave effects into the model, the sediment movement exhibited hysteresis as discussed in Section 3.1. This phenomenon was attributed to the storm-induced BSS surpassing the CSS, leading to the resuspension of sediment from the seabed. Commonly, enhanced wave–current dynamics and BSS during typhoons are the main reasons for the sharp increase in SSC. It was found that sediment is exchanged between channels and shoals during typhoon events, thereby influencing SSC distribution for up to 1 month, as indicated by satellite imagery [67].

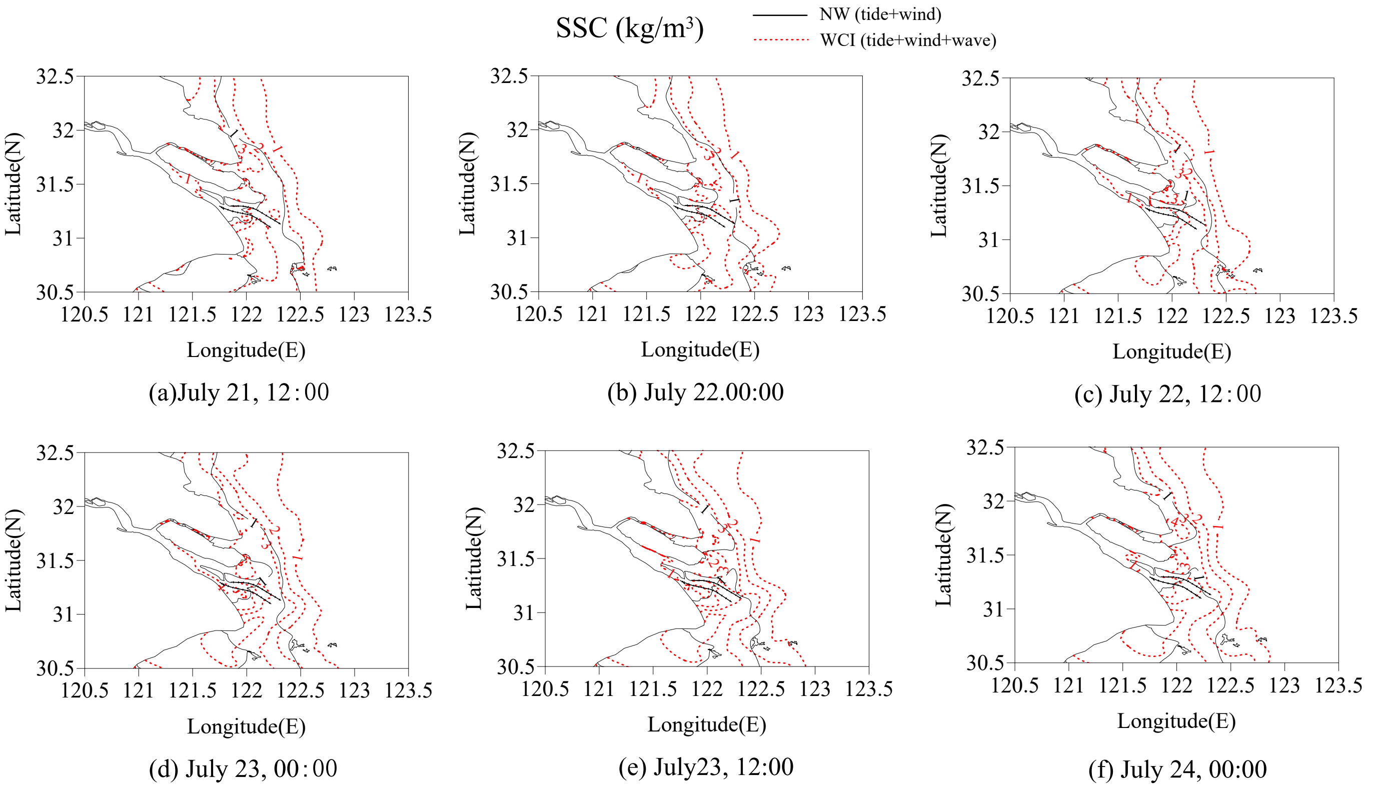

(a)July 21, 12:00 (b) July 22.00:00 (c) July 22, 12:00

(d) July 23, 00:00 (e) July23, 12:00 (f) July 24, 00:00

Figure 16. Comparison of predicted suspended sediment concentration (SSC) isoline for WCI (tide + wind + wave) and NW (tide + wind) forcing conditions as described in Table 3.

Besides the horizontal distribution of SSC, it is imperative to quantify the impact of wave action on the vertical mixing of sediment. It is widely recognized that waves influence suspended sediment transport and resuspension by changing the flow velocity and direction. A previous study showed that during rising tides, the vertical gradient of SSC was small, with an L-shaped distribution, which is closely related to wave action [68]. Furthermore, waves can significantly alter the upper ocean structure and thus affect the vertical distribution of SSC through mechanisms of breaking and non-breaking-induced mixing [69]. The vertical SSC profiles at all study sites at the time when the typhoon landed at 12:00 on 22 July are depicted in Figure 17. These profiles primarily exhibited vertical-line patterns as proposed by Van Rijn (1993), with the remainder following an exponential trend (NBD and SCD), signifying effective water mixing under the influence of strong winds and waves. Compared to the two conditions, after adding the wave stress, the SSC increased significantly at all points, which provided evidence that the current did not cause strong resuspension, while waves play a crucial role in sediment resuspension. Despite the relatively lesser impact of strong winds and large waves in the inner channels compared to offshore regions, these areas still experienced the effects of the typhoon. At NBD and SCD, characterized by shallow water geometries, the bottom SSC significantly surpassed the surface SSC, implying that the BSS exceeded the CSS and that sediment would be released from the bottom into the water column.

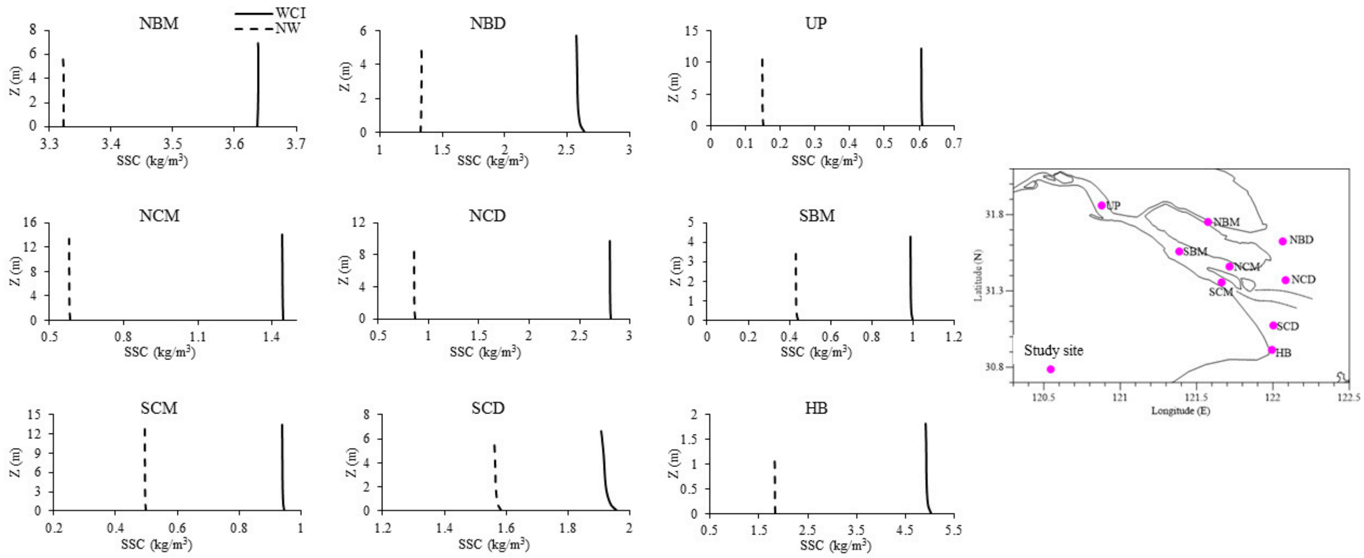

Figure 17. The vertical profile of suspended sediment concentration (SSC) form at the nine study sites indicated in Figure 1 at 12:00 on 22 July 2018.

In summary, the role of currents in sediment transport primarily involves them serving as a dynamic carrier to propel sediment movement. Waves are the primary factor in altering the sediment concentration by enhancing water column turbulence near the bed and strengthening the BSS to facilitate the resuspension of bottom sediment.

4.2. Storm Wave-Induced SSC Variation

Given that tide is another important contributing factor to sediment transport, we conducted the simulation (Table 2, condition 1) without consideration of wind and waves. Figure 18 illustrates a comparison of SSC for tide only (AT) and tide + wind + wave (WCI) by calculating the difference. The impact of storm waves on SSC transport was noteworthy, showcasing both positive and negative influences attributed to the rapid fluctuations in wind strength during the typhoon period. The effects of typhoons on SSC difference distributions were significant in the offshore shallow water. Furthermore, the decrease in SSC post typhoon passage occurred at a slower rate compared to the increase in SSC prior to the typhoon's arrival. However, the alteration in SSC difference resulting from wind and wave action in the inner channels remained almost zero, suggesting that tides significantly dominate SSC dynamics. This phenomenon demonstrates the pivotal role of storm waves in triggering the resuspension of sediment during typhoon events in the most studied areas.

Considering the importance of BSS in sediment resuspension, the comparison between the predicted BSS for the WCI and AT scenarios in the three groups of study sites is shown in Figure 19.

In comparing the impact of storm wave action on BBS, the difference between these two scenarios is evident. Under the influence of tide alone (Condition 1), the BSS exhibits minimal change throughout the typhoon period. However, upon incorporating wind and wave forces (Condition 3), the BSS exhibits a continuous increase as the typhoon approaches the study area prior to and during typhoon landfall, followed by a gradual decline post landfall. Particularly at the NBD site, the maximum BSS recorded under Condition 3 (tide + wind + wave) significantly surpasses that of Condition 1 (tide only). This indicates that storm waves play a pivotal role in driving the BSS to exceed the CSS, thereby facilitating the resuspension of sediment in the estuary.

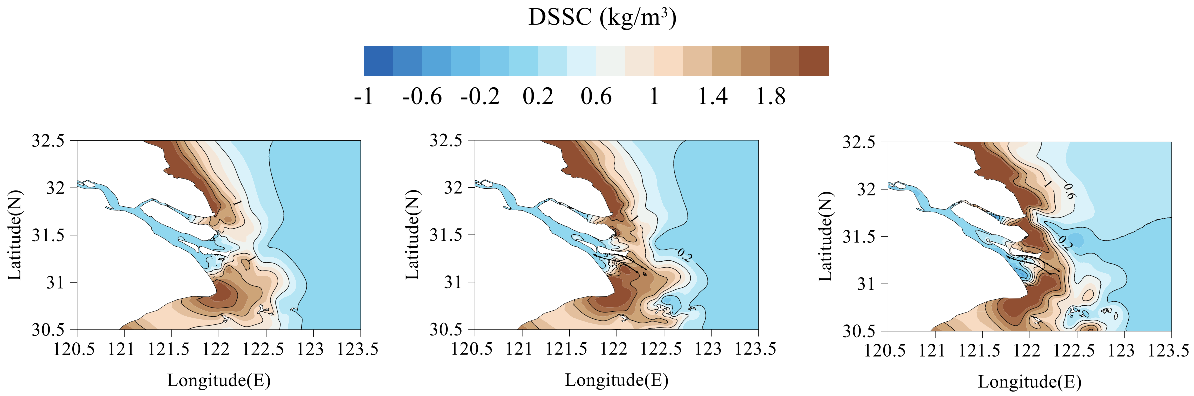

(a)July 21, 12 : 00 (b) July 22.00:00 (c) July 22, 12 : 00

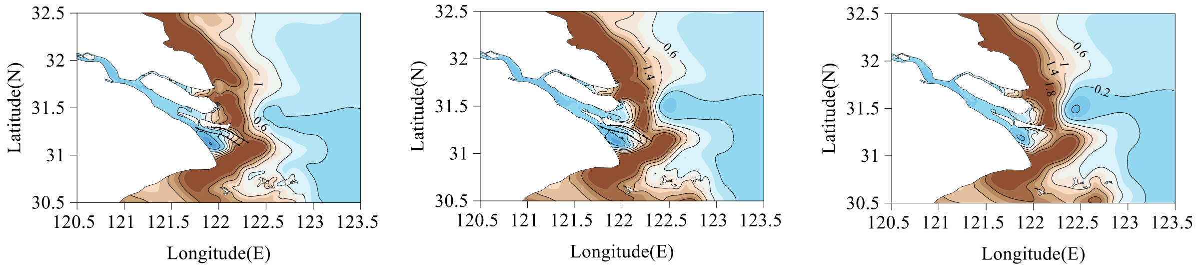

(d) July 23, 00 : 00 (e) July23, 12:00 (f) July 24, 00:00

Figure 18. The difference between the predicted SSC difference (DSSC) distribution for WCI (tide + wind + wave) and AT (tidal only) forcing conditions as described in Table 3.

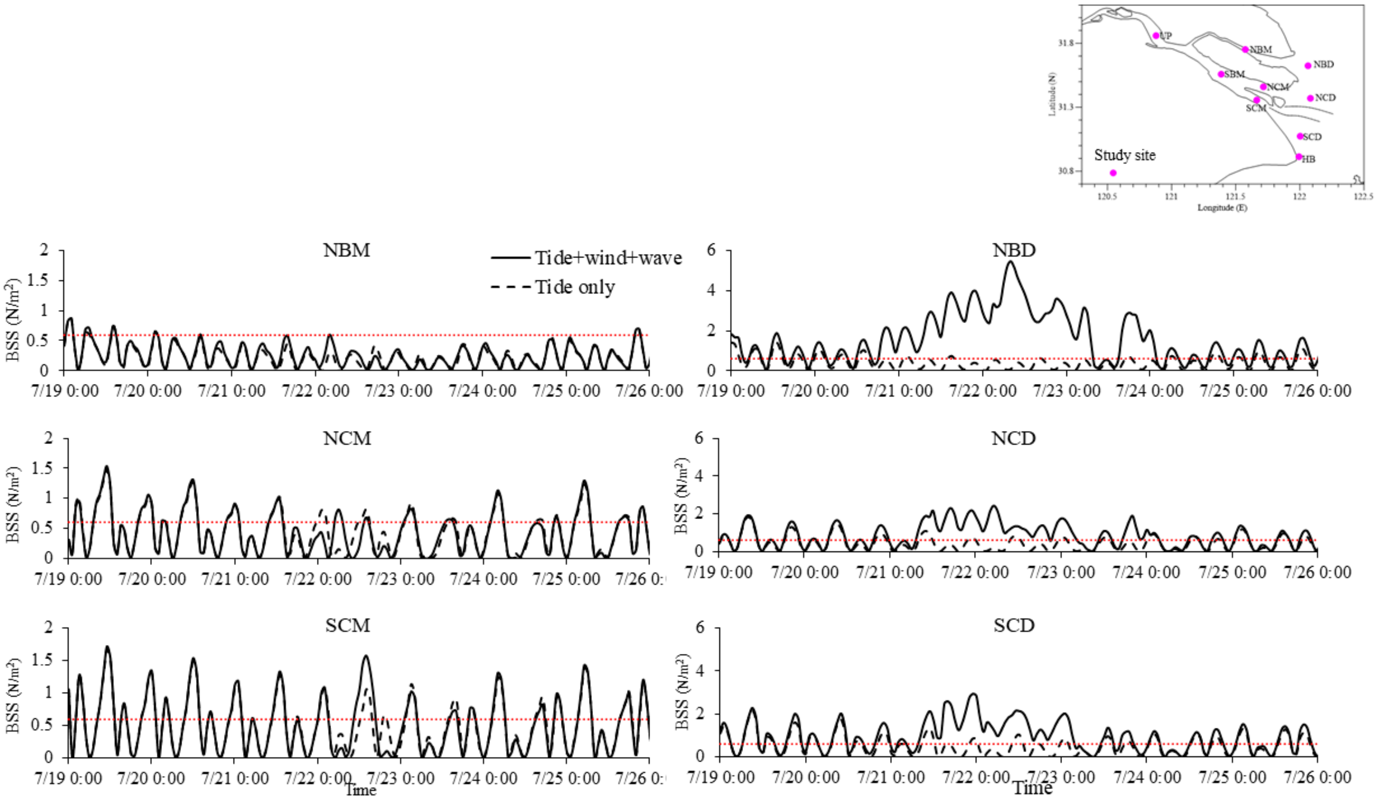

Figure 19. Comparison of bed shear stress (BSS) between the WCI (tide + wind + wave) and AT (tide only) conditions at the six study sites in the three main branches indicated in Figure 1.

In comparing the SSC at all points, the SSC displayed distinct patterns in the inner channels and the offshore area. Differences in SSC with and without waves at the study sites in the channel occurred predominantly during the period of typhoon landfall, with them being maintained for roughly 24 h. Apart from this time interval, minimal differences were observed in SSC between the conditions with and without wave effects. However, the SSC in offshore regions exhibited a more pronounced and longer-lasting duration. The maximum values can reach 5.67 N/m^2, 2.98 N/m^2, and 3.12 N/m^2 at the three offshore points, representing a substantial increase of approximately 845%, 397%, and 420% respectively, compared to the tide-only condition. This demonstrates that offshore areas directly exposed to the open sea are more sensitive to the effects of storm waves. A previous study by Lu et al. (2019) [64] also compared wave and non-wave conditions and found that the entire area of Zhoushan had higher BSS during Typhoon Fungwong, which presented a similar mechanism to that in the present study.

5. Conclusions

This study focuses on the horizontal and vertical variation in SSC during Typhoon Ampil by coupling a wave and hydrodynamic model with a sediment transport module based on MIKE 3. The model was verified by the measured water level, current speed and direction, wave height and period, and SSC in the study area. To investigate the mechanism and relative importance of the major driving forces of the SSC, simulations were conducted for tide only, tide + wind, and tide + wind + wave forcing conditions during the typhoon period. The main conclusions are summarized below:

During Typhoon Ampil, heightened turbulence and SSC in the upper water column were observed across the majority of the study area. Among the selected six study sites, NBD experienced a significant peak SSC of 3.8 kg/m^3 during the typhoon event, marking a 52% increase from normal levels. Similarly, NCD exhibited a notable 90% increase, reaching a peak SSC of 3.3 kg/m^3, while NCM recorded a 33.3% elevation to 1.6 kg/m^3. The impact on SSC at the remaining study sites was changed slightly by the typhoon, attributed to their relative positioning with respect to the typhoon's path. Meanwhile, the peak BSS coincided with typhoon landfall but displayed a quicker rate of change compared to SSC, particularly evident at the outer mouth of the estuary. This suggests that the typhoon not only elevated BSS to initiate sediment release from the seabed but also enhanced sediment exchange between the seabed and the water column. The time lag between BSS and SSC can be attributed to hysteresis behavior in sediment exchange, where sediment in the water column requires additional time to settle back down to the seabed before resuspension occurs. The wind and wave effects are weak in the inner study sites due to the shallow water depth and narrow channel width so that BSS remains below the CSS, with SSC primarily influenced by tidal currents rather than wind and wave forces.

Typhoon Ampil enhanced the turbidity maximum zone in the coastal shoal area out of the estuarine mouth of YRE. Analysis of the horizontal distribution of SSC revealed that elevated SSC at HB moved with the current to the mouth of the South Passage, subsequently progressing to the North Passage and North Channel. Typhoon-induced increases in BBS surpassed the CSS, leading to the resuspension of bottom sediment into the water column. Meanwhile, strong wind and waves also enhanced the turbulence near the bed and vertical mixing, therefore accelerating the exchange frequency and intensity between deposition and suspended sediment. The peak BBS occurred outside the estuarine mouth, corresponding with the turbidity maximum zone, proving that the increased SSC in this area primarily came from sediment resuspension. The vertical profiles of SSC exhibited exponential and vertical-line characteristics during the typhoon period, indicating minimal disparity between surface and bottom sediment concentrations except within the estuarine mouth area, where the storm could alter the vertical SSC structure. The NPL area experienced significant sediment exchange between deposition and suspended sediment, attributed to the complex hydrodynamics resulting from the construction of the Deep-Water Channel Project, characterized by strong currents and greater water depths.

Three scenarios were conducted for tide only (AT), tide + wind (NW), and tide + wind + wave (WCI) forcing conditions during the typhoon period in this study. Comparisons of model results for NW and WCI revealed a notable increase in SSC by 2 kg/m^3 upon the addition of wave forcing, with the offshore area experiencing an approximately 20 times rise. In addition, the recovery time for NW was found to be similar to the typhoon period, while WCI exhibited hysteresis behavior. The comparisons between WCI and AT highlighted the negligible impact of storm wave-induced SSC in the channels but emphasized its significance in the offshore regions. Storm waves are the major contributing factor of BSS in the offshore area where the peak BSS can achieve 5.67 N/m^2, 2.98 N/m^2, and 3.12 N/m^2 at NBD, NCD, and SCD, respectively, under the condition of WCI.

Although this study presents a comprehensive analysis of the key dynamics affecting SSC under typhoon influence across different scenarios using numerical modeling, several important questions remain unresolved and should be paid more attention in the future. The YRE is one of the most representative mesotidal estuaries in the world, whose matter exchange and dominating dynamics are highly complicated due to its multi-branch geometry. As the area is vulnerable to typhoon attacks, the morphological change in the YRE is an important consideration which is not included herein but will be the focus of our future study. In addition, the turbidity current caused by salinity and high sediment concentrations is also an important future subject that we will investigate further.

Author Contributions: Conceptualization completed by J.W. and C.K.; methodology proposed by J.W., C.K. and D.F.; field data measured by D.F.; simulations conducted by J.W. and W.X.; validation made by D.F. and J.W.; writing—original draft preparation, J.W.; writing—review and editing, C.K., R.Q. and Q.Z.; funding acquisition provided by D.F. and R.Q. All authors have read and agreed to the published version of the manuscript.

Funding: This research was funded by the Innovation Program of Shanghai Municipal Education Commission (2021-01-07-00-07-E00093) and the Interdisciplinary Project in Ocean Research of Tongji University (2022-2-ZD-04).

Data Availability Statement: Data are contained within the article.

Acknowledgments: We are sincerely grateful to Fan Daidu, Qin Rufu, and Kuo Chen for supporting the fieldwork and measured data for model validation.

Conflicts of Interest: The authors declare no conflicts of interest.

References

1. Van der Wal, D.; Pye, K.; Neal, A. Long-term morphological change in the Ribble estuary, Northwest England. *Mar. Geol.* **2002**, *189*, 249–266. [CrossRef]
2. Xie, D.; Zou, Q.-P.; Mignone, A.; MacRae, J.D. Coastal flooding from wave overtopping and sea level rise adaptation in the northeastern USA. *Coast. Eng.* **2019**, *150*, 39–58. [CrossRef]
3. Aalst, M.V. The impacts of climate change on the risk of natural disasters. *Disasters* **2006**, *30*, 5–18. [CrossRef] [PubMed]
4. Gao, Y.; Li, B.; Feng, Z.; Zuo, X. Global climate change and geological disaster response analysis. *J. Geomech.* **2017**, *23*, 65–77.
5. Oppenheimer, M. A Physical Science Perspective on Disaster: Through the Prism of Global Warming. *Soc. Res. Int. Q.* **2008**, *75*, 659–668. [CrossRef]
6. Jiang, T.; Shi, Y.F. Global climatic warming: The Yangtze floods and potential loss. *Adv. Earth Sci.* **2003**, *18*, 277–284.
7. Chou, J.M.; Dong, W.J.; Xu, H.; Ban, J.H. Assessment on Economic Losses of Tropical Cyclone Disasters Affecting China's Coastal Areas. *Meteoro Log. Environ. Sci.* **2022**, *45*, 1–10.
8. Sui, G.J.; Tang, D.L. Typhoon Disasters and Regional Economic Divergence: Evidence from Guangdong. *Macroeconomy* **2012**, *220*, 18–25.
9. Ren, Z.; Liu, C.; Ou, Y.; Zhang, P.; Fan, H.; Zhao, X.; Cheng, H.; Teng, L.; Tang, M.; Zhou, F. Deep Learning-Based Simulation of Surface Suspended Sediment Concentration in the Yangtze Estuary during Typhoon In-Fa. *Water* **2024**, *16*, 146. [CrossRef]
10. Yang, J.K. *The Impact of Typhoon on Economic Growth in Coastal Areas of China*; Jilin University: Jilin, China, 2022.
11. Liu, J.Q.; Yin, P.; Gao, F.; Chen, B.; Lian, E.G. Water H-O isotopic characteristics of Nandu River and their response to typhoon Kalmaegi. *Mar. Geol. Quat. Geol.* **2018**, *38*, 171–177.
12. Bai, Y.B.; Shi, J.Y.; Lu, C.T.; Zhang, G.J.; Ding, W. Spatio-temporal distribution characteristics of surge in the reach below Nantong of Yangtze Estuary under the influence of Typhoon In-Fa. *Hydro-Sci. Eng.* **2021**, *6*, 25–33.

13. Ren, J.B.; He, Q.; Shen, J.; Xu, F.; Guo, L.C.; Xie, W.M.; Zhu, L. The effect mechanism of a remote typhoon "Sanba" on wave dynamics in the Changjiang Estuary. *Mar. Sci.* **2020**, *44*, 12–23.
14. Sun, D.Y.; Tong, C.; Chen, K.L.; Lin, X.; Huang, J.F. Effects of typhoon Dujuan on contents of Nutrrient in Soil Pore water of marshes and tidal water in Min River Estuary. *Wetl. Sci.* **2017**, *16*, 809–817.
15. Feng, S.Z. The advance of Researches on storm surge. *World Sci-Tech R&D* **1998**, *20*, 44–47.
16. Yang, S.-L.; Eisma, D.; Ding, P.-X. Sedimentary processes on an estuarine marsh island within the turbidity maximum zone of the Yangtze River mouth. *Geo-Mar. Lett.* **2000**, *20*, 87–92. [CrossRef]
17. Bai, Y.; Wang, Z.; Shen, H. Three-dimensional modelling of sediment transport and the effects of dredging in the Haihe estuary. *Estuar. Coast. Shelf Sci.* **2003**, *56*, 175–186. [CrossRef]
18. Pontee, N.; Whitehead, P.; Hayes, C. The effect of freshwater flow on siltation in the Humber estuary, North East UK. *Estuar. Coast. Shelf Sci.* **2004**, *60*, 241–249. [CrossRef]
19. Perillo, G.M.; Syvitski, J.P. Mechanisms of sediment retention in estuaries. *Estuar. Coast. Shelf Sci.* **2010**, *87*, 175–176. [CrossRef]
20. Luan, H.L.; Ding, P.X.; Wang, Z.B.; Ge, J.Z.; Yang, S.L. Decadal morphological evolution of the Yangtze River estuary in response to river input changes and estuarine engineering projects. *Geomorphology* **2016**, *265*, 12–23. [CrossRef]
21. Wei, W.; Mei, X.; Dai, Z.; Tang, Z. Recent morphodynamic evolution of the largest uninhibited island in the Yangtze (Changjiang) estuary during 1998–2014: Influence of the anthropogenic interference. *Cont. Shelf Res.* **2016**, *124*, 83–94. [CrossRef]
22. Yang, S.; Fan, J.; Shi, B.; Bouma, T.; Xu, K.; Yang, H.; Zhang, S.; Zhu, Q.; Shi, X. Remote impacts of typhoons on the hydrodynamics, sediment transport and bed stability of an intertidal wetland in the Yangtze Delta. *J. Hydrol.* **2019**, *575*, 755–766. [CrossRef]
23. Shen, H.; Zhang, C. Mixing of salt water and fresh water in the Changjiang River estuary and its effects on suspended sediment. *Chin. Geogr. Sci.* **1992**, *2*, 373–381. [CrossRef]
24. Chen, S.; Zhang, G.; Yang, S. Temporal and spatial changes of suspended sediment concentration and resuspension in the Yangtze River estuary. *J. Geogr. Sci.* **2003**, *13*, 498–506.
25. Pang, C.; Zhao, E.; Yang, Y. Numerical simulation on the process of salt- water intrusion and its impact on the suspended sediment concentration in the Changjiang (Yangtze) estuary. *Chin. J. Oceanol. Limnol.* **2010**, *28*, 609–618. [CrossRef]
26. Wu, H.; Zhu, J.; Choi, B.H. Links between saltwater intrusion and subtidal cir- culation in the Changjiang Estuary: A model-guided study. *Cont. Shelf Res.* **2010**, *30*, 1891–1905. [CrossRef]
27. Shen, F.; Zhou, Y.; Li, J.; He, Q.; Verhoef, W. Remotely sensed variability of the suspended sediment concentration and its response to decreased river discharge in the Yangtze estuary and adjacent coast. *Cont. Shelf Res.* **2013**, *69*, 52–61. [CrossRef]
28. Hennings, I.; Herbers, D. Suspended sediment signatures induced by shallow water undulating bottom topography. *Remote Sens. Environ.* **2014**, *140*, 294–305. [CrossRef]
29. Schoellhamer, D.H. Anthropogenic Sediment Resuspension Mechanisms in a Shallow Microtidal Estuary. *Estuar. Coast. Shelf Sci.* **1996**, *43*, 533–548. [CrossRef]
30. He, X.; Bai, Y.; Pan, D.; Huang, N.; Dong, X.; Chen, J.; Chen, C.T.; Cui, Q. Using geostationary satellite ocean color data to map the diurnal dynamics of suspended particulate matter in coastal waters. *Remote Sens. Environ.* **2013**, *133*, 225–239. [CrossRef]
31. Xu, H.-J.; Huang, Z.; Bai, Y.-C.; Su, L.-S.; Hong, Y.-C.; Lu, T.-T.; Wang, X. Numerical analysis of sediment deposition in Yangtze River estuary: Insight from conceptual estuary models. *Appl. Ocean Res.* **2020**, *104*, 102372. [CrossRef]
32. Wang, S.; Zhang, G.; Fu, D. Numerical simulation of tides, tidal currents, residual current and shear front in estuary. *Period. Ocean Univ. China* **2010**, *40*, 31–40. (In Chinese)
33. Huang, M.F.; Montgomery, D.R. Altered regional sediment trans- port regime after a large typhoon, southern Taiwan. *Geology* **2013**, *41*, 1223–1226. [CrossRef]
34. Miles, T.; Glenn, S.M.; Schofield, O. Temporal and spatial variability in fall storm induced sediment resuspension on the Mid-Atlantic Bight. *Cont. Shelf Res.* **2013**, *63*, S36–S49. [CrossRef]
35. Jiang, X.; Lu, B.; He, Y. Response of the turbidity maximum zone to fluctuations in sediment discharge from river to estuary in the Changjiang Estuary (China). *Estuar. Coast. Shelf Sci.* **2013**, *131*, 24–30. [CrossRef]
36. Bian, C.; Jiang, W.; Quan, Q.; Wang, T.; Greatbatch, R.J.; Li, W. Distributions of suspended sediment concentration in the Yellow Sea and the East China Sea based on field surveys during the four seasons of 2011. *J. Mar. Syst.* **2013**, *121–122*, 24–35. [CrossRef]
37. Li, Y.; Li, X. Remote sensing observations and numerical studies of a super typhoon-induced suspended sediment concentration variation in the East China Sea. *Ocean Model.* **2016**, *104*, 187–202. [CrossRef]
38. Yan, Q.S. Overview of the storm-generated deposits on nearshore zone and open shelf. *Oceanol. Limnol. Sin.* **1984**, *15*, 14–20. (In Chinese)
39. Suanez, S.; Cariolet, J.-M.; Cancouët, R.; Ardhuin, F.; Delacourt, C. Dune recovery after storm erosion on a high-energy beach: Vougot Beach, Brittany (France). *Geomorphology* **2012**, *139–140*, 16–33. [CrossRef]
40. Wainright, S.C. Sediment-to-water fluxes of particulate material and microbes by resuspension and their contribution to the planktonic food web. *Mar. Ecol. Prog. Ser.* **1990**, *62*, 271–281. [CrossRef]
41. Chen, Z.; Yu, L.; Gupta, A. The Yangtze River: An introduction. *Geomorphology* **2001**, *41*, 73–75. [CrossRef]
42. Yang, S.L.; Zhang, J.; Dai, S.B.; Li, M.; Xu, X.J. Effect of deposition and erosion within the main river channel and large lakes on sediment delivery to the estuary of the Yangtze River. *J. Geophys. Res. Earth Surf.* **2007**, *112*, F02005. [CrossRef]
43. Shen, Q.; Huang, W.; Qi, D. Integrated Modeling of Typhoon Damrey's Effects on Sediment Resuspension and Transport in the North Passage of Changjiang Estuary, China. *J. Waterw. Port Coast. Ocean Eng.* **2018**, *144*, 4018011–4018015. [CrossRef]

44. Syvitski, J.P.M.; Kettner, A.J.; Overeem, I.; Hutton, E.W.H.; Hannon, M.T.; Brakenridge, G.R.; Day, J.; Vörösmarty, C.; Saito, Y.; Giosan, L.; et al. Sinking deltas of human activities. *Nat. Geosci.* **2009**, *2*, 681–686. [CrossRef]
45. Ma, F.; Jiang, C.; Rauen, W.B.; Lin, B. Modelling sediment transport processes in a macro-tidal estuary. *Sci. China Technol. Sci.* **2009**, *52*, 3368–3375. [CrossRef]
46. Zhu, L.; He, Q.; Shen, J.; Wang, Y. The influence of human activities on morphodynamics and alteration of sediment source and sink in the Changjiang Estuary. *Geomorphology* **2016**, *273*, 52–62. [CrossRef]
47. Mulligan, R.P.; Hay, A.E.; Bowen, A.J. Wave-driven circulation in a coastal bay during the landfall of a hurricane. *J. Geophys. Res. Ocean.* **2008**, *113*, C05026. [CrossRef]
48. DHI Group. *Mike 21 & Mike 3 FLOW MODEL FM. Hydrodynamic and Transport Module Scientific Documentation*; DHI Group: Hørsholm, Denmark, 2021.
49. Chen, W.; Chen, K.; Kuang, C.; Zhu, D.Z.; He, L.; Mao, X.; Liang, H.; Song, H. Influence of sea level rise on saline water intrusion in the Yangtze River Estuary. China. *Appl. Ocean Res.* **2016**, *54*, 12–25. [CrossRef]
50. Ren, J.B. *Wave Dynamics and Its Impact on Sediment Transport under Typhoons in the Changjiang Estuary*; East China Normal University: Shanghai, China, 2020. (In Chinese)
51. Wang, J.; Kuang, C.; Chen, K.; Fan, D.; Qin, R.; Han, X. Wave–Current Interaction by Typhoon Fongwong on Saline Water Intrusion and Vertical Stratification in the Yangtze River Estuary. *Estuar. Coast. Shelf Sci.* **2022**, *279*, 108138. [CrossRef]
52. Li, Z.; Li, S.; Hou, Y.; Mo, D.; Li, J.; Yin, B. Typhoon-induced wind waves in the northern East China Sea during two typhoon events: The impact of wind field and wave-current interaction. *J. Oceanol. Limnol.* **2022**, *40*, 934–949. [CrossRef]
53. Fan, Y.S. *Seabed Erosion and Its Mechanism in the Littoral Area of Yellow River Delta*; East China Normal University: Shanghai, China, 2019. (In Chinese)
54. Zhang, Z.; Wu, H.; Yin, X.; Qiao, F. Dynamical response of Changjiang River plume to a severe Typhoon with the surface wave-induced mixing. *J. Geophys. Res. Ocean.* **2018**, *123*, 9369–9388. [CrossRef]
55. Willmott, C.J. On the validation of models. *Phys. Geogr.* **1981**, *2*, 184–194. [CrossRef]
56. Wang, J.; Kuang, C.; Cheng, S.; Fan, D.; Chen, K.; Chen, J. The Responses of Storm Surges to Representative Typhoons under Wave-Current Interaction in the Yangtze River Estuary. *J. Mar. Sci. Eng.* **2024**, *12*, 90. [CrossRef]
57. Liang, M.; Liu, J.; Lin, Y.; He, Z.; Wei, W.; Jia, L. Typhoon-induced suspended sediment dynamics in the mouth-bar region of a river/wave-dominated estuary. *Mar. Geol.* **2023**, *456*, 106972. [CrossRef]
58. Gao, A.; Zhao, H.Y.; Yang, S.L.; Dai, S.H.; Chen, S.L.; Li, P. Seasonal and tidal variations in suspended sediment concentration under the influence of river runoff, tidal current and wind waves. *Adv. Mar. Sci.* **2008**, *26*, 44–50. (In Chinese)
59. Fan, J.Q. *Influence of Typhoon on Sedimentary Dynamic Process of Intertidal Wetland in Yangtze Estuary*; East China Normal University: Shanghai, China, 2019.
60. Rijn, L.C.V. *Principles of Sediment Transport in Rivers, Estuaries and Coastal Seas*; Morfologie Morf.; Aqua Publications: Madison, WI, USA, 1993.
61. Liu, H.; He, Q.; Wang, Z.; Weltje, G.J.; Zhang, J. Dynamics and spatial variability of near-bottom sediment exchange in the Yangtze Estuary, China. *Estuar. Coast. Shelf Sci.* **2010**, *86*, 322–330. [CrossRef]
62. Li, X.; Leonardi, N.; Plater, A.J. Wave-driven sediment resuspension and salt marsh frontal erosion alter the export of sediments from macro-tidal estuaries. *Geomorphology* **2019**, *325*, 17–28. [CrossRef]
63. Xu, L.D. *Fully Coupled Numerical Modelling of Sediment Transport and Bed Change under Currents and Waves Influences*; Zhejiang University: Hangzhou, China, 2019.
64. Lu, H.F.; Gu, F.F.; Chen, X.E.; Qi, D.M. Effect of sea waves on sediment transport in the sea waters surrounding Zhoushan Islands, China. *Period. Ocean Univ. China* **2019**, *49*, 1–9.
65. Zou, Q.; Hay, A.E. The vertical structure of the wave bottom boundary layer over a sloping bed: Theory and field measurements. *J. Phys. Oceanogr.* **2003**, *33*, 1380–1400. [CrossRef]
66. Lu, J.; Jiang, J.B.; Li, A.C.; Ma, X.C. Impact of Typhoon Chan-hom on the marine environment and sediment dynamics on the inner shelf of the East China Sea: In-situ seafloor observations. *Mar. Geol.* **2018**, *406*, 72–83. [CrossRef]
67. Tang, R.; Shen, F.; Ge, J.; Yang, S.; Gao, W. Investigating typhoon impact on SSC through hourly satellite and real-time field observations: A case study of the Yangtze estuary. *Cont. Shelf Res.* **2021**, *224*, 104475. [CrossRef]
68. Shi, Z.; Ling, H.L. Vertical profiles of fine suspension concentration in the Changjiang Estuary. *J. Sediment Res.* **1999**, *2*, 59–64.
69. Cu, Y.T.; Rong, Z.R. Effects of Breaking and Non-Breaking Surface Wave Mixingon the Changjiang River Plume Dynamics in Summer. *J. Geophys. Res. Ocean.* **2023**, *128*, e2022JC019501.